Response of 3D printed lattice-based spinal fusion cages to static and dynamic loading

Jaka Pižorn

Technische Universiteit Delft

TU Delft

Response of 3D printed lattice-based spinal fusion cages to static and dynamic loading

by

Jaka Pižorn

to obtain the degree of Master of Science
at the Delft University of Technology,

Student number: 4744411
Specialization: Biomaterials and Tissue Biomechanics,
Biomedical Engineering MSc programme,
Department of Biomechanical Engineering,
Faculty of Mechanical, Maritime and Materials Engineering,
Delft University of Technology

Supervisors: Dr. Jie Zhou, TU Delft
Prof. dr. Stephen J. Ferguson, ETH Zurich

An electronic version of this thesis is available at `http://repository.tudelft.nl/`.

TU Delft

Abstract

Back pain is a major economic problem that can dramatically affect the quality of life. There are many causes that can lead to back pain, but intervertebral disc degeneration is a recognised cause, with many pathophysiologies causing the disc to behave abnormally. The harmful effect of whole-body vibration (WBV) environment on the human intervertebral disc has been demonstrated to have an increased relative risk of up to 19% compared to no exposure to WBV, with the risk of failure even in healthy discs. One of the treatments for a degenerative disc is spinal fusion procedure, in which the human intervertebral disc is replaced by a spinal fusion cage. In this thesis, the influence of WBV on custom-made spinal fusion cages was investigated.
With the advent of additive manufacturing, which has become increasingly available and precise over the years, lattice-based scaffolds were designed as spinal fusion implants and manufactured using a Polyet 3D printer. The influence of the unit cell design on the build quality and the quasi-static mechanical properties as well as the dynamic WBV reaction was observed. Therefore, four different unit cell types were designed: body-centered cube (BC cube), face-centered cube (FX cube), truncated octahedron (T octa) and negative Poisson cube (NP cube). The influence of 3D printing direction and scaffold porosity on print quality and mechanical properties were also investigated.
The build quality was determined by measuring the nominal size, determining the beam diameter and using CT. The quasi-static mechanical properties were determined with the compression test, for which the elastic modulus and stiffness were determined and compared. The dynamic response to WBV was determined with a mechanical test setup that imitates a base excitation model. In order to test scaffolds with this test set-up, two cylindrical bases were added and printed as one sample together with the scaffold. The bases were embedded and mounted in the testing cups. A constant sinusoidal displacement to the lower embedding cup was applied and using accelerometers, the accelerations of the input and response were measured. The difference between the response and input was compared and observed at which frequency the sample broke or reached the highest gain. This was done for all samples and the influence of unit cell type, 3D-printing direction and porosity on the dynamic response was observed.
Although there were certain defects and deviations from the designed scaffolds, the build quality of the additive manufacturing technique chosen was adequate. The direction of 3D printing had the greatest influence on the build quality, while the type of unit cell and porosity had a less obvious influence.
The compression test provided insight into which unit cell types have a higher elastic modulus, that the 3D printing direction perpendicular to the test direction achieved higher E values, and that higher porosity, which is desirable for implants, resulted in a lower Young's modulus.
In terms of the dynamic response, the results of this work indicate that the FX cube design is the most robust and would improve the safety of the implant when exposed to WBV. For the 3D printing direction, it may be concluded that the perpendicular direction, i.e. the layers are perpendicular to the test direction, can best withstand the dynamic forces. The increase in porosity from 50% to 70% showed a decrease in resistance to the dynamic loading, with scaffolds failing more often and at lower frequencies. Therefore, the unit cell design, 3D printing direction and porosity should be important in the design of lattice-based spinal implants that are designed to withstand WBV. The precision and consistency achieved through the manufacturing process is also an important part of the build quality and mechanical properties for producing reliable and safe implants. Understanding how different designs and porosity of the spinal fusion scaffolds influence the resistance to WBV conditions will help to develop safe and resistant implants which replace degenerated natural intervertebral discs.

Acknowledgments

I would like to thank my family for the constant support in my journey leading up to this master thesis. Especially to my father and mother, who encouraged and backed me for all my ambitions, thank you.
To my dear Rok, I will be forever grateful for your trust and support that you give while I am pursuing my goals.
I would also like to thank my supervisors: Dr. Zhou at TU Delft, for the help and thorough support throughout my master thesis and Prof. Ferguson at ETH Zurich, for giving me the chance to come to Zurich and work on this project while also providing me with everything I needed for my thesis.
To Bastian, Dmitriy, Matthias, Pascal and Philipp, thank you for helping me on my project when I got stuck. Thank you Hanna for the help with the CT scans and for all the time we spend in the lab. Also to the rest of the laboratory at ETH, in which I conducted the thesis, I would like to thank everyone for the help as well as everyday support.
Jung-Chew Tse at the Engineering Design and Computing Laboratory provided his expertise with quality 3D printing of my samples. Lastly I would like to thank Paul Egan for letting me use his code and giving good advice for my project.

Jaka Pižorn

Contents

Abstract iii

Acknowledgments iv

1 Introduction 1
- 1.1 Intervertebral disc . . . 1
  - 1.1.1 Structure and function . . . 1
  - 1.1.2 Aging of the IVD and its consequences . . . 3
  - 1.1.3 Degeneration of the IVD and its consequences . . . 3
  - 1.1.4 Quasi-static mechanical loading . . . 4
  - 1.1.5 Dynamic mechanical loading . . . 5
- 1.2 Treatments of a degenerated disc . . . 6
- 1.3 Spinal fusion implants . . . 6
  - 1.3.1 Types and functions of spinal fusion implants . . . 7
  - 1.3.2 Quasi-static mechanical tests on spinal fusion implants . . . 8
  - 1.3.3 Dynamic mechanical tests on spinal fusion implants . . . 8
- 1.4 Aim of the study . . . 9

2 Materials and Methods 10
- 2.1 Design of lattice structure . . . 10
- 2.2 3D printing . . . 12
- 2.3 Embedding of Samples . . . 13
- 2.4 Mechanical testing . . . 14
  - 2.4.1 Quasi-Static compression test . . . 15
  - 2.4.2 Dynamic test . . . 15
- 2.5 Statistical analysis . . . 16

3 Results 17
- 3.1 Build accuracy . . . 17
- 3.2 Compression test . . . 22
- 3.3 Dynamic response . . . 25

4 Discussion 28
- 4.1 Sample characterisation . . . 28
- 4.2 Compression test . . . 30
- 4.3 Dynamic response . . . 31
- 4.4 Future perspectives . . . 33

5 Conclusion 34

6 Abbreviations 36

A Appendix 37

B Appendix 38

C Appendix 40

D Appendix 41

E Appendix 43

F Appendix 47

Bibliography 53

1 Introduction

The human vertebral column serves as the axial support of the trunk, transfers the upper body weight to the lower limbs and protects the spinal cord [1]. It has a complex structure compiling several components, each of which is important for the vertebral column to function normally. A healthy spine can withstand normal forces and it also allows extension, flexion and rotation of the trunk.
Although many of us do not have back pain problems, 1-4% of new cases of back pain per year and a prevalence of 5-10% (percent of population at any given time) are reported [2], with about 70 to 85% of the Western population developing lower back pain at least once during their lifetime [3]. Chronic back pain, which is often a major financial burden and severely affects the lives and daily activities of patients, is estimated to affect 19% of adult Europeans [4]. Low back pain (LBP) is recognised as a huge financial burden, costing over $100 billion annually in the US [5]. To help people who live with chronic back pain or who have a lower quality of life due to various problems in the human spine, and to reduce the financial burden on the health care system, much research has been done on spinal problems and their solutions.

The cause of LBP is multifactorial, but intervertebral disc (IVD) related conditions, resulting from ageing, disease or injury, have been a major contributing factor [6]. There are several approaches to treating LBP, ranging from non-invasive to surgical procedures. In some treatments, the disc is replaced by an artificial implant, which depending on the type of implant, promotes spinal fusion or functionally replaces the IVD. In such cases where the disc is replaced by spinal implants, special care must be taken to ensure the implant withstands the conditions and does not fail, which in turn causes more problems than it solves. In 2016, the market for spinal implants was worth over $6.8 billion [7], so there is an economic interest in finding an appropriate solution.
Understanding the mechanical and biological interactions between the spinal implants and the spine is essential for a long-term safe medical treatment. With a profound insight into the implants, this will hopefully lead to novel spinal implants when the natural discs have failed.

1.1. Intervertebral disc

1.1.1. Structure and function

The IVD is part of the spine, which is divided into 5 sections (Figure 1.1a), in a S-shape from the side, running from the cervical region at the top to the coccyx distally. The lower sections carry more upper body weight and experience higher loads than the upper sections but allow less or no movement compared to the higher vertebrae. The difference in function is reflected in the size and geometry of the vertebrae, as they become larger in every section of the spine towards the sacrum [1].

The IVD is the largest avascular structure in the human body of an adult [10], located between two bony vertebrae and accounting for up to 1/3 of the vertebral column's height [11]. Figure 1.1b shows a functional spinal unit (FSU), also known as the motion unit. It is often used as a model of the spine, as it still has biomechanical properties comparable to the entire vertebral column [12]. The FSU, a representation of the entire spine, consists of 2 vertebral bodies, between them an IVD and surrounded by several ligaments.
The overall size of an IVD varies from one spinal region to another but in the lumbar region, which is often used for research, the measurements of IVDs report that the widest part is $55.9 \pm 9.4 mm$ lateral and the narrow

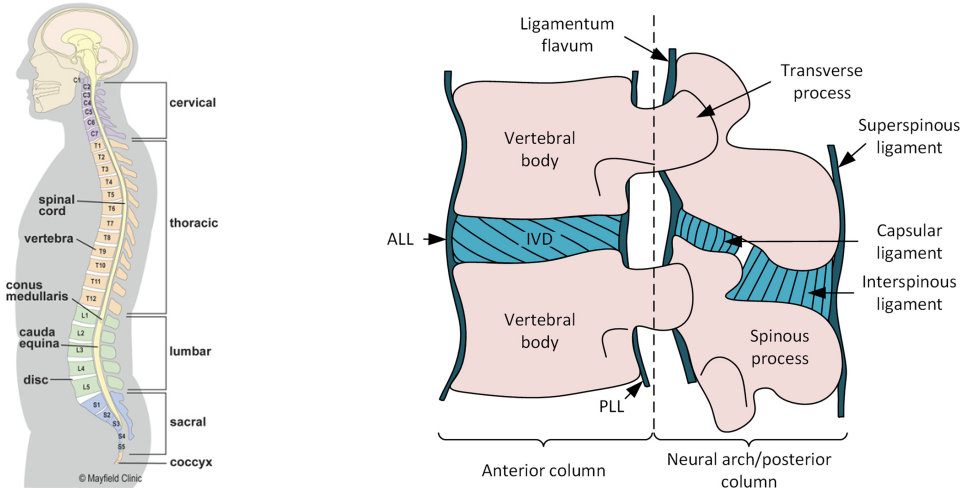

(a) (b)

Figure 1.1: a) The human spinal column [8]. b) Graphical depiction of the FSU [9].

part $37.2 \pm 4.7 mm$ anteroposterior, while the height is between from 7.1 to 12.5 mm [13].
The structure of an IVD consists of three integral interconnected tissues (Figure 1.2), the Nucleus pulposus (NP) in the center, surrounded by Annulus fibrosis (AF), and cartilaginous end plates (CEP) cranial and caudal, which connect the IVD together with AF fibres to the bony vertebral body [14].

NP is composed of randomly organised collagen fibres and radially oriented elastin fibres both nested in a highly hydrated aggrecan-containing gel [11] with a water content of 70-90% [12].
The surrounding AF is a complex of 15 to 25 concentric rings, called lamellae, containing obliquely oriented, regularly arranged collagen fibre bundles of a narrow outer zone and a wider inner zone of fibrocartilage encompassing the NP [15]. These fibres lie parallel to their own lamella [14]. It has been observed that the number of layers per annulus increases in the lower lumbar spine levels [10] and also depends on age. Within a lamella, these fibres are oriented around 60° to the vertical axis, interchanging to the left and right in adjacent lamellae [11].
The CEP mainly consists out of hyaline cartilage and chondrocyte cells, which are about 1 mm thick and are the thinnest in the center for the transport of nutrients to the intervertebral disc [10].

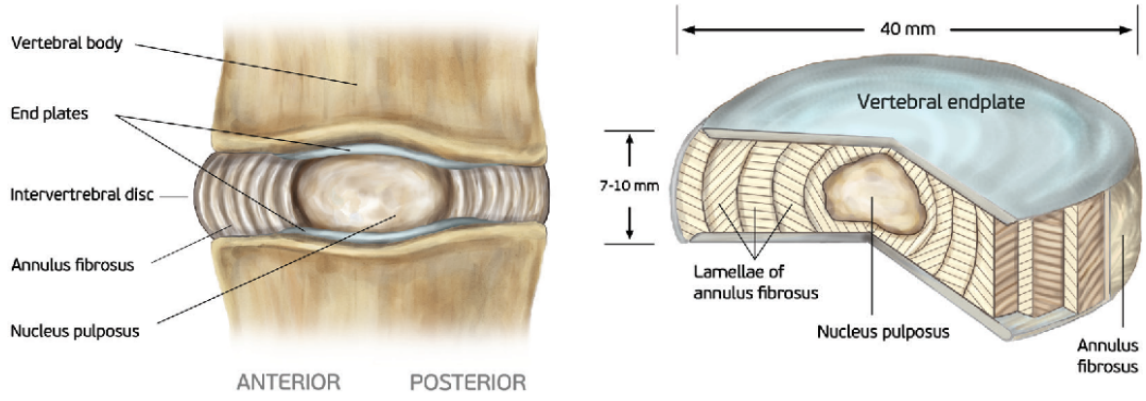

(a) (b)

Figure 1.2: a) Anatomy of a FSU without ligaments. b) Structure of the IVD [16].

The function of the IVD is only possible because of its complex structure. The effectiveness of the IVD depends on the coherence of the annulus and nucleus. If we place the disc under compression (Figure 1.3a), it

causes the pressure to rise inside the NP, which in turn is transferred to the surrounding AF. The tension in the annulus increases and prevents the nucleus from expanding further. The pressure inside the NP is then exerted on the vertebral end plates. The compression is taken up partly by the nucleus and partly by the annulus, while the pressure on the endplates transfers the load to the next vertebral body [17]. The annulus also connects successive vertebrae and resembles a woven strap to resist tension and torsion [1]. AF, together with the ligaments and muscles, enables the vertebral column flexion, extension and, to a lesser extent, lateral bending of the spine. If one component of the IVD malfunctions, the annulus-nucleus alliance breaks down, leading to an abnormal IVD.

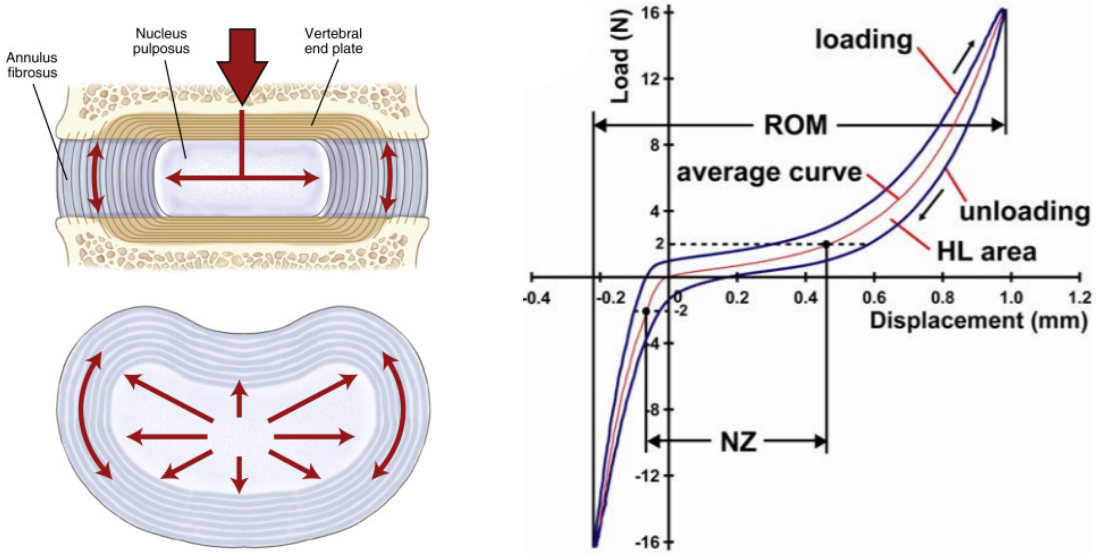

(a) (b)

Figure 1.3: a) The human spinal column [8]. b) Compression-Tension load-displacement curve for the IVD [18].

1.1.2. Aging of the IVD and its consequences

All IVD structures change with age, which leads to different mechanical properties and may eventually lead to some deviations from physiological function. This change in IVD is often clinically referred to as Degenerative Disc Disease (DDD) [19].

The collagen in the AF increases in quantity, but the amount of elastic fibres decreases. The nucleus shows one of the most fundamental changes [17], as the concentration of proteoglycans decreases significantly, from about 65% of dry weight in early adulthood to about 30% by the age of 60 [20]. There is also more collagen and collagen-proteoglcyan binding. The NP begins to have AF properties that make the difference between the NP and AF less obvious. It has been observed that the cartilaginous end plate changes with age in such a way that it decreases in both thickness and diameter and is slowly replaced by bone [10, 12]. Since the bony vertebral body carries the load transferred from the IVD, it is important to note that with age, bone density decreases, with horizontal trabecular being absorbed. The consequence is that the cortical bone must carry more of the load transmitted by the IVD. However, this could lead to injury, as the cortical bone can only withstand 2% of deformation, compared to 9.5% for trabecular bone [10, 17].

With increasing age, the NP changes, causing the entire disc to become stiffer and the majority of the load is transferred through the AF. The intervertebral disc adapts to this new situation by ossifying both the AF fibre and the CEP, with the aim of creating a larger surface to distribute the axial load. The ossification and less water in the intervertebral disc lead to greater hysteresis, less damping and a reduction in spinal column movement [17].

1.1.3. Degeneration of the IVD and its consequences

Degeneration refers to abnormal changes due to diseases or injuries of the intervertebral disc or its surrounding structures.

Internal disc disruption (IDD) is a widely and well understood cause of back pain caused by an internal dis-

ruption of the normal structural and biochemical integrity of the symptomatic disc[21, 22]. IDD (Figure 1.4a) can be identified by the degradation of the NP and presence of radial fissures into which NP infiltrates [17]. It is not the same as disc herniation, as the NP does not protrude through the AF. Disc herniation (DH) (as seen in Figure 1.4b) is a term used when, typically the NP or AF are displaced beyond the physiological IVD space. Herniation, like the IDD, can disrupt the surrounding nerves in the spinal canal, but also the nerves in the outer layers of the annulus, both of which often cause back pain.
The examination of herniated discs [23] has shown that in a healthy disc under extreme axial compression load the first structures to yield are the fibres in the middle of the disc wall or the end plate. Other injuries can occur if excessive torsion or lateral shear are applied, which can additionally lead to circumferential tears in the AF layers [17].
As discussed in Chapter 1.1.5, dynamic loading stiffens the intervertebral disc due to water loss, while the damping effect of the NP is smaller. This can lead to intervertebral disc injury as a fatigue failure of the end plate, whereby allowing the nucleus to protrude into the vertebrae. When the body experiences whole body vibrations from the environment, it has been observed that at resonant frequencies of the human intervertebral disc [24], sudden load shocks have led to failure of the IVD. Environments where WBV has been observed are typical for truck drivers or other such heavy vehicles, working around heavy machinery where vibrations are transferred through the floor and mine workers. This is dangerous as this can happen not only in a degenerated IVD but also in a healthy one.

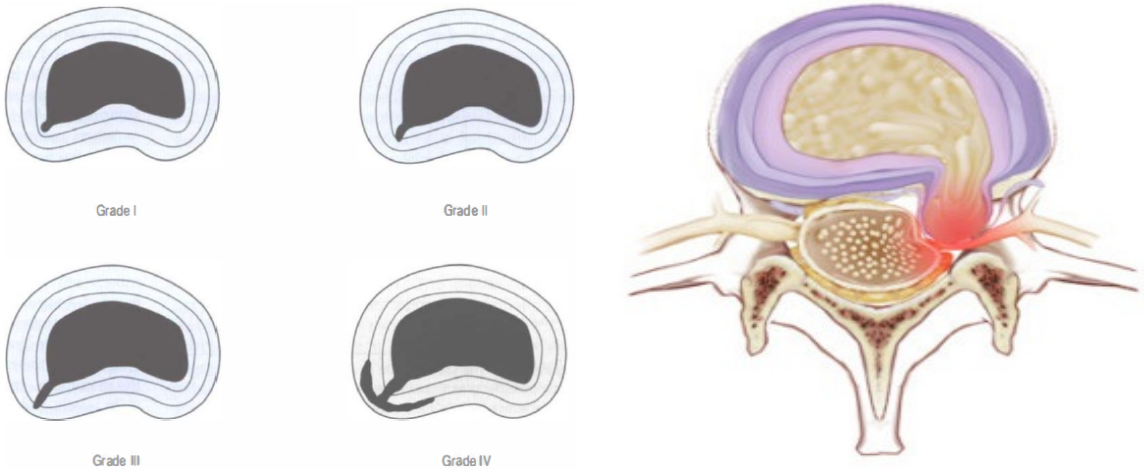

(a) (b)

Figure 1.4: a) IDD at different stages classified as grades [17]. b) Herniated disc, where it is clearly seen how the NP protrudes through the AF, in this case onto the spinal nerve [25].

1.1.4. Quasi-static mechanical loading

The disc as a whole is a nonlinear viscoelastic structure with a strain rate that affects the response of the IVD [9]. When the strain rate is increased, the disc exhibits a stiffer response due to its viscous part. A load-displacement curve of the IVD under compression-tension loading is shown in Figure 1.3b. Normally, the test is preformed up to physiological loads applied in both directions to precondition the IVD, the result of which is that the curves do not change significantly between cycles [26]. The tests are most commonly performed on the lumbar IVD under uniaxial compression. A typical response is shown in Figure 1.3b under physiological load, where a hysteresis between loading and unloading is clearly visible and the difference between the initial and final height of the IVD can be measured. This hysteresis tells us how much energy has been lost due to the displacement of proteoglycans and water and the repositioning and rupture of collagen fibres [17]. The curve is composed of two zones, the first being the neutral zone (NZ) and the second elastic zone (EZ). The NZ is the part of the range of motion within which spinal movement takes place with minimal internal resistance [17] and is the part of the load-displacement curve where the load change is minimal compared to the displacement. The elastic deformation occurs beyond the neutral zone and goes up to the maximum load, in compression and tension. The elastic zone together with the NZ forms the range of motion (ROM) of the IVD. It can also be observed that the elastic part does not exhibit a real linear change, but has a nonlinear

response. Therefore sometimes the curve is divided in parts, for which the stiffness or elastic modulus is then locally determined.
Creep, a phenomenon in which at a constant stress on the IVD the strain continues to increase and the height of the IVD decreases, is exhibited in the IVD and is often used to determine if the IVD is degraded. A degraded disc has a faster creep rate.
The intervertebral disc is stiffer under compression than under tension, which is due to the increase in hydrostatic pressure that occurs in the NP if under compressive load. The intervertebral disc is anisotropic, made specifically such, to manage the loads to which it is exposed as efficiently as possible, although this peculiarity of the mechanical properties may mean that it cannot cope with other loads adequately [12].

1.1.5. Dynamic mechanical loading

While the quasi-static properties have been extensively studied, the dynamic side is less understood and the effects on the IVD and the whole spine are not clear. Everyday activities such as walking, running and traveling in vehicles are an everyday source of whole body vibrations with a frequency ranging from 5HZ to 30Hz [27]. Higher frequencies can occur in industry, where workers may be exposed to vibrations that travel from machines across the floor to their legs and up to the spine.
When the intervertebral disc is under cyclic dynamic load, it was observed that hysteresis decreases. In a recent study [28], when two uniaxial quasi-static tests were performed in succession, they saw that the hysteresis of the second cycle was smaller than that of the first. This could mean that the intervertebral disc was not able to withstand repetitive loads and could therefore fail.
The low frequency (below 10Hz) response to pure and combined cyclic loading [29–31] was observed and the creep and viscoelastic properties of the human IVD were analysed. While this provides an insight into tissue properties at low frequencies, the boundary conditions and loads applied to the IVD are not physiological, since both the preload and the dynamic load, were applied from the top of the IVD. Therefore, in a broad frequency range, the whole body vibration (WBV) applied from the bottom, like a base excitation model, is a closer simulation of the physiological loads and conditions of the IVD. It has been observed that WBV affects the disc, its height change and mechanical properties, while also associated with lower back pain [24]. When performing WBV in a base excitation setting, the upper body mass (and possibly additional weight due to the work-specific task) is applied on the superior side of the IVD, while a dynamic (sinusoidal) stimuli is forced on the inferior side, mimicking the high frequency stimulation of vibrations imposed by machines or the environment [32] (such a setup is shown in Figure 1.5a).

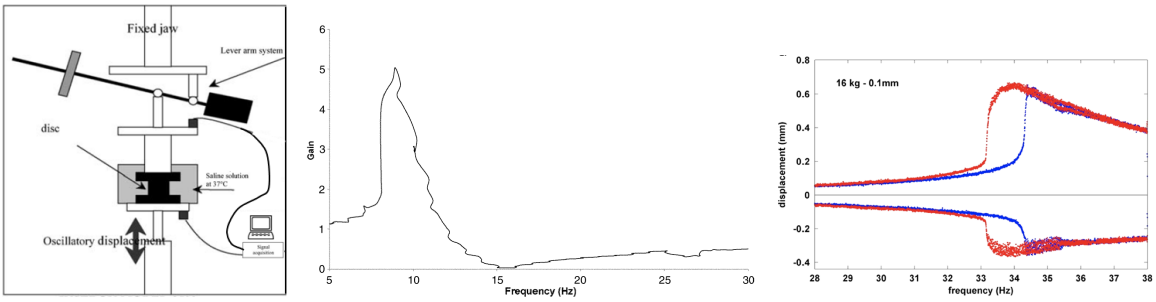

(a) (b) (c)

Figure 1.5: a) A setup which mimics WBV (Figure adopted and changed from [27]). b) A typical response of the IVD when under WBV shown as gain over a frequency range [27]. c) Response of an IVD to a continuous frequency sweep under WBV, in blue the increasing frequency sweep (IFS) and in red the decreasing frequency sweep (DFS). The jump phenomenon is visible around 34.5Hz for the IFS and around 33.5Hz for the DFS [24].

Some studies have focused on mimicking WBV conditions at discrete [27] (bath), (air)[33] or continuous frequency [24](air), mainly observing how the amplitude and applied preload (upper body mass) affect disc response. With higher preload, the resonant frequency of the disc decreased, which was also the case when higher amplitudes were applied. A typical response of such a test at a selected preload and amplitude is shown in Figure 1.5b. The resonant frequency of the human intervertebral disc varied from 8Hz [27] to 40.9Hz [24].
In the study by Marini[24] the experiments were carried out in such a way that for a given preload a constant displacement was forced in the form of a sinusoidal wave. Then a continuous frequency sweep was performed upwards and again downwards. Then the displacement was changed at the same preload. Finally,

the experiment was repeated for different preloads. The author of the study came to the conclusion that the disc exhibited non-linear asymmetric properties during a continuous frequency sweep. The response differed between the increasing and decreasing frequency sweeps, while at the same time exhibiting abrupt oscillatory changes at different frequencies, which were refereed to as the jump phenomenon (Figure 1.5c), with adverse effects on the IVD. The failure of the end plate was evident in many IVD samples after exposure to WBV. The change of the preload and amplitude of the input stimulation affected the response, but in a way that it moved the point of the resonant frequency. While Kasra [33] pointed out the stiffening effect at a higher frequency, Marini [24] showed hardening and softening effects.
Although the results of various studies have not provided a fully conclusive answer to what exactly causes the IVD failure under WBV and which parameters are most influential, the EU directive 2002/44/EC describes the safety requirements with regard to the exposure of workers to vibration [34]. It sets daily limits for exposure to WBV.

1.2. Treatments of a degenerated disc

The treatment depends on the cause and severity of the degeneration or injury.
It can be treated with conservative methods such as physiotherapy and exercise. This strengthens the surrounding soft tissues and relieves the IVD of some pressure. However this is often not sufficient and invasive methods are used. One such method is epidural injections, which are often used for chronic discogenic pain [19].
Spinal Decompression is one of the most frequently performed spinal operations [35], in which parts of the ligaments and disc fragments are removed to relieve the pressure on the nerves.
Spinal fusion (Figure 1.6a) is a well-established surgical method that is performed when the disc is considered the main cause of back pain and non-invasive methods have not helped. It is a procedure in which the natural disc is usually removed and a bone graft, bone graft substitute or implant, often called an interbody cage, is placed between the vertebrae [36]. Stabilizing rods and screws are frequently used to connect the two vertebrae.

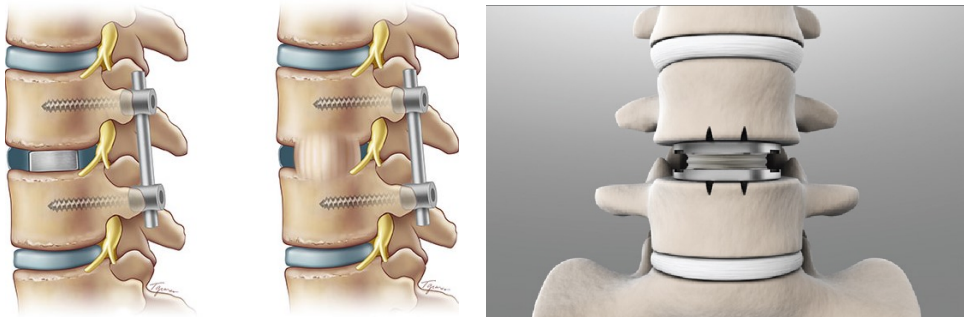

(a) (b)

Figure 1.6: a) Spinal fusion, with a cage between the vertebrae and rod-screws, after the surgery on the left and after bone in-growth on the right [37]. b) Artificial disc replacement implant in a human spine[38].

Artificial disc replacement (ADR), also known as total disc replacement (TDR), is a surgical procedure that restores the anatomy and function of the affected spine [36] (Figure 1.6b), in contrast to spinal fusion, where the physiological motion of the FSU is gone. There are many different designs and materials used for this, ranging from concave-convex couples, ball and socket/trough, beam based lattice designs, with materials ranging from metal on metal, metal on polyethylene, to ceramic on ceramic [36].

1.3. Spinal fusion implants

As described in the previous section, there are different ways of treating a degenerated human IVD depending on the severity and type of injury or disease. Although ADR is the new trend in the development of IVD implants, conventional spinal fusion is still widely used. Because ADR devices are relatively new, there are still some mechanical mechanical properties and long-term effects which are less understood. Some disadvantages compared to fusion devices have been mentioned, such as the increased potential for displacement or component failure [39], while at the same time there are more implant-related complications and higher

rates of reoperation than with spinal fusion devices or posterior surgical procedure (PP) [40].
Spinal fusion is considered the gold standard in treatment of many IVD related problems, and the number of spinal fusion procedures has increased markedly, with the number doubling in the US from 1997 to 2010 [35]. For the reasons mentioned above, spinal fusion device is the focus of this master thesis. There are several criteria that a spinal fusion cage must meet. If spinal fusion is performed, the fixation must ensure stability for the entire spine as well as for the affected FSU. The cage must be biocompatible, inert and should promotethe ingrowth of bone tissue. The elastic modulus of the cage has to be in the region of the surrounding bone, ensuring not to over stress the bone at the bone-implant interface. However, we must bear in mind that a spinal cage is not the only implanted bearing device, with peddicle screws and rods providing a lot of support and stability. The cage itself has an important role as a scaffold to bridge the gap between adjacent vertebra. The primary function of the cage is to be a primary stabilization device that holds the spine in place and allows secondary stability to occur, with osteointegration and osteoconductivity of the cage being important for the overall success of the procedure [41].

1.3.1. Types and functions of spinal fusion implants

There are several materials, designs and concepts for spinal cages. There are three elements that are important for a good fusion of the adjacent vertebrae. The presence of precursor cells capable of differentiating into osteoblasts, a osteoconductive scaffold into which the cells can grow, and growth factors that promote the transformation of precursor cells into osteoblasts [35].
Autologous bone graft, which is often harvested from the iliac crest [42], is considered beneficial because it contains all of the above fusion-promoting elements. However, there are problems with these grafts because of the high morbidity associated with the harvest and limited availability of such grafts [35], as well as the negative effects of additional surgery to harvest the graft from the patient.
Over the years, many different designs made of different materials have been studied and used for spinal fusion (Figure 1.7). A metal cage is often used, produced out of Magnesium, Titanium and Tantalum for example, with empty volume spaces and surface features. Typically, bone or bone substitute material is filled into the empty volumes of the implants to promote bone growth.
Figure 1.7a shows a cage made of implant-grade titanium alloy (Ti-6Al-4V) with surface features for securing the implant in the upper and lower vertebral body. The empty void in the centre can be filled with bone growth promoting material. A screw cage design (Figure 1.7b) is screwed into the area of the removed IVD and is often used in pairs. The screw motion secures the implant while the empty centre of the screw is filled with bone graft. Similar designs can also be made out of different polymers (Figure 1.7c), such as PEEK, PC, medical photopolymers and composites. In Figure 1.7d the design has a combination of two different materials, Mg and expanded PCL within the metal structure.

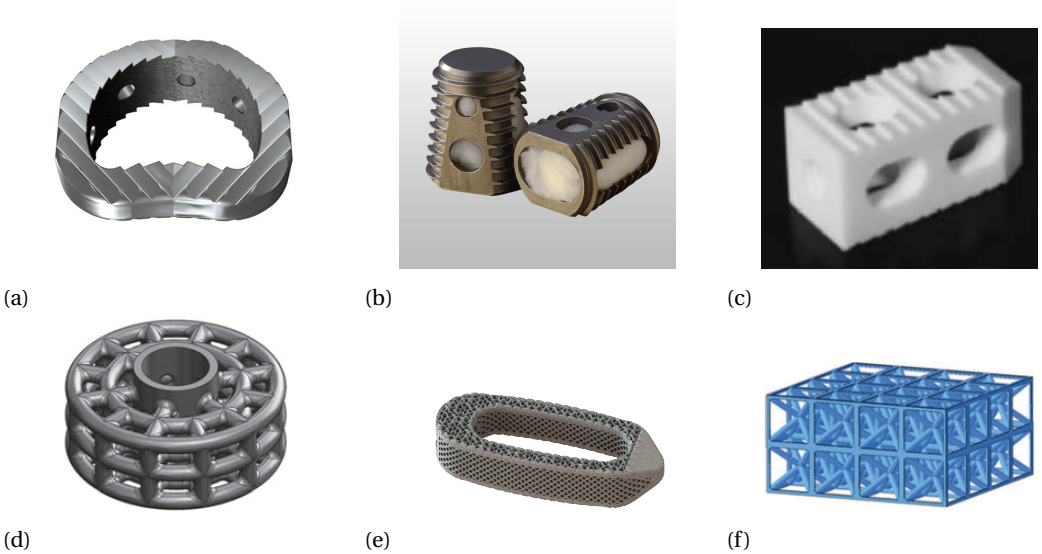

(a) (b) (c)

(d) (e) (f)

Figure 1.7: a) Interbody fusion cage made out of implant-grade titanium alloy [43]. b) Screw design fusion cage, filled with bone graft [44]. c) An open cage design machined out of a composite [45]. d) Mg spinal fusion cage, optionally filled with expanded PCL [46]. e) An example of a titanium beam-based lattice design implant [47]. f) Lattice cage 3D printed out of a biomedical photopolymer [48].

While all the designs described above are commonly used, spinal cages that have a controllable porous structure while providing adequate stability are highly desirable because a porous structure with appropriate pore size promotes bone formation [49]. Since the introduction of high-precision 3D printers, it has been possible to manufacture such small, highly porous, patterned designs, which are important for vascularization and minelarisation. Porosity greater than 50% is favourable [50], as high porosity in scaffolds promotes vascular growth and facilitates nutrient transport, such as oxygen [51]. The pore size should be between 200μm, with the smaller pore being beneficial for tissue growth for faster filling of cavities, and up to about 800μm for vascularization and nutrient transport [49]. In Figure 1.7e, a 3D-printed titanium truss based cage shows a similar overall design to conventionally manufactured cages, but the lattice structure provides a high porosity for nutrient transport and bone ingrowth. With cages like these, it may not be necessary to add bone graft, as the permeability is so high that the cells and nutrients should be able to come from the surrounding tissue. However, titanium has a high elastic modulus and the design would therefore need very large pores to reduce its overall stiffness. High stiffness may prompt stress shielding and inhibit bone growth [48]. Therefore, 3D-printed lattice cage designs using biocompatible polymers studied by Egan [48, 49, 51] are of interest because polymers have a lower elastic modulus but it is possible to maintain the desired porosity and pore size (Figure 1.7f). Egan investigated how a lattice based unit cell design may affect the mechanical properties and biological properties [48]. He discovered that the stiffness is not affected by a different pattern of the same unit cells but that different batches of 3D printed samples show larger differences [48]. It was found that the body centred unit cell is most favourable overall because it has high porosity, a high shear modulus and surface-volume ratio for the required elastic modulus compared to other unit cells studied. However, other unit cells may have some advantageous properties, especially under dynamic loads, which was not investigated. If the fabrication process, structural design, mechanical properties of the scaffold and design performance are combined, a favourable design for regenerative medicine may be developed [51].
3D printing allows us to produce designs with negative Poisson's ratio while maintaining good porosity and pore size, which has been shown to be beneficial for medical implants [52–54]. For use in the spine for damaged disc replacement, the idea was that negative Poisson's ratio would allow a similar range of motion to natural IVD while preventing the implant from blocking the surrounding nerve when under compression because the implant does not bulge [53]. An auxetic unit cell can be easily developed from 2D to 3D design [55] and patterned to provide a useful overall nominal size design for implantation.
When determining the mechanical properties of spinal implants, 3D printing allows us to take into account the mechanical test setup required to perform the tests in question. Especially when tensile forces are to be applied to the implants, an FSU-like structure can be designed to mimic the IVD-vertebra interface.

1.3.2. Quasi-static mechanical tests on spinal fusion implants

From a literature study performed on the mechanical characterization of spinal implants, it was found that the most commonly performed test on the spinal cage was a compression test. The ASTM 2077 standard [56] specifies how compression, compression-shear and torsion experiments should be performed and which parameters should be used. Although there is an ASTM standard test method for intervertebral body fusion devices, a proprietary test method is often used [46, 57–59], which usually consists of two flat surfaces between which the implant is compressed. The test parameters, especially the crosshead speed, vary between the studies. There are studies in which a whole vertebral column or FSU, either human [60] or animal [61] with an inserted implant, has been used to conduct quasi-static tests. While this provides valuable insight into the properties of the fusion device implanted in biological tissue, the results of these tests may not give the correct properties of the implant itself. Therefore, if the goal is to characterize the spinal implant itself, a rigid test setup should be used.
The modulus of elasticity, stiffness and yield point are often determined from the tests performed, allowing comparison of different fusion device designs, materials and the interaction with surrounding tissues in the spine.

1.3.3. Dynamic mechanical tests on spinal fusion implants

Fatigue tests on spinal implants are usually performed to determine the response to dynamic tests. Although ASTM F2077 standard [56] specifies the test method for dynamic testing, others have developed their own test methods [45, 57, 58] that are similar to the standard. The test parameters, such as test frequency, loads and run-out cycles, and test setup varied from study to study. The test environment has usually been air, but a wet environment has also been employed [45].
The aim of the fatigue test is to determine how many cycles at a certain load it takes for the implant to fail.

The test is usually carried out for different loads until the implant fails before the specified number of cycles (known as run-out). An S-N curve can be plotted, and the endurance limit determined. The results of the fatigue test indicate whether the implant is safe under physiological loads and the conditions that it will experience for the expected implanted lifetime.
The fatigue test is important and valuable for determining the safety of the implant, but as described in section 1.1.5, harmful WBV effects as observed by Marini [24] have not been investigated. A broad frequency range of a sinusoidal displacement imposed on the implant in a base-excitation-like model with observation of how different properties of the implant can change the response could be important, as the detrimental effects of these conditions have been observed at frequencies ranging from around 34-40Hz [24]. Therefore it would be useful to consider these properties when designing and manufacturing spinal implants.

1.4. Aim of the study

The aim of the master thesis was the production of lattice design spinal cages which are 3D-printed and examined for mechanical properties, especially under WBV conditions. In the laboratory where the thesis was conducted the knowledge of lattice design spinal cages and the harmful effects of WBV on human IVD have been studied. The lattice design implants studied by Egan [48–51, 62] have shown promise, particularly for spinal fusion, while Marini [24, 63, 64] has demonstrated the detrimental effects of WBV on the human disc. Therefore combining the findings to investigate the lattice cage design, manufacturing, quasi-static properties and effects of VBW was a natural step.
The main objective was to design lattice spinal cages with different unit cells, changing porosity and 3D-printing direction. It had to simulate the position and conditions in the spine while allowing to test for the mechanical properties and observing the response of detrimental WBV conditions.
The research questions for this study were defined as:

- How to manufacture a lattice spinal cage design, for which quasi-static mechanical properties and behaviour under WBV can be observed?
- How do different unit cells influence the 3D printing, mechanical properties and WBV response?
- How does the 3D printing direction of the lattice spinal cage influence the 3D printing, mechanical properties and WBV response?
- How does the porosity of the lattice spinal cage influence the 3D printing, mechanical properties, and WBV response?
- What is the response of the lattice spinal cages when using a base excitation model for a broad frequency range simulating WBV conditions, and is it similar to the response of the human IVD?
- Which design parameters improve the safety of the lattice spinal cages for WBV conditions?

From the above research questions, the main objectives of the research are clear. Design, manufacture and examine the 3D-printed lattice spinal cages. Determine their mechanical properties and their response to WBV conditions. These findings will be used to investigate the safety and importance of observing how WBV conditions affect the lattice design implants and hopefully provide valuable insights.

2

Materials and Methods

2.1. Design of lattice structure

The design of the unit cells, the building blocks of the scaffolds, was chosen to meet the desired properties, porosity and mechanical properties as described in chapter 1.3. A single unit cell, defined by the truss diameter ϕ and the cell length L_c, was patterned into a 5x5x2 (width x depth x height) scaffold. A cylindrical base ($\phi = 30mm$, height=$20mm$) was added at the top and bottom, which acts similar to the vertebral body (Figure 2.1). The base-scaffold-base construct resembles the FSU and is especially important when conducting the dynamic test, because if the scaffold is to be under tension, and if there were no connection to the base, no tension forces would be possible on the scaffold.

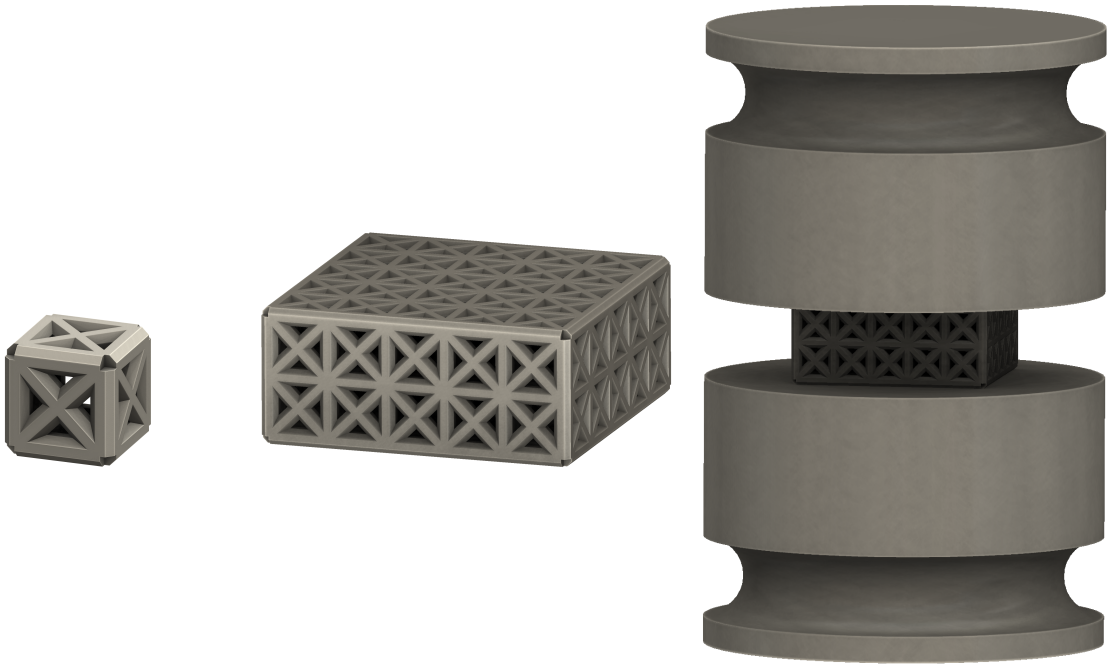

(a) (b) (c)

Figure 2.1: CAD models of: a) a single unit cell (FX-cube), b) a scaffold of 5x5x2 patterned unit cells, c) a testing sample made out of two bases on top and bottom of the scaffold.

Four different unit cells were selected (Figure 2.2): Body Centered Cube (BC-cube), Face Centered Cube (FX-cube), Truncated Octahedron (T-octa), and Negative Poisson's Cube (NP-cube). The first three unit cells were chosen based on the findings of Egan [48–50, 62, 65], where they showed good mechanical properties while having a good surface-to-volume ratio and at high porosity. The NP-cube in general was chosen, because we

wanted to observe how a unit cell with negative Poisson's ratio responds to dynamic loading, while the specific type of the NP-cube was chosen because if it's simplicity to go from 2D to 3D. All unit cells, except for the Negative Poisson's ratio unit cell, were designed using Python code, with permission, from the previous work of Paul Egan, which automated Abaqus software to generate lattice structures with user-defined properties. The user can define the unit cell type, truss diameter and porosity. The unit cell can be patterned in all three directions to obtain the desired size.
For the Negative Poisson's ratio unit cell, the geometry was created in Solidworks, while the theoretical Poisson's ratio and porosity were calculated in Matlab.

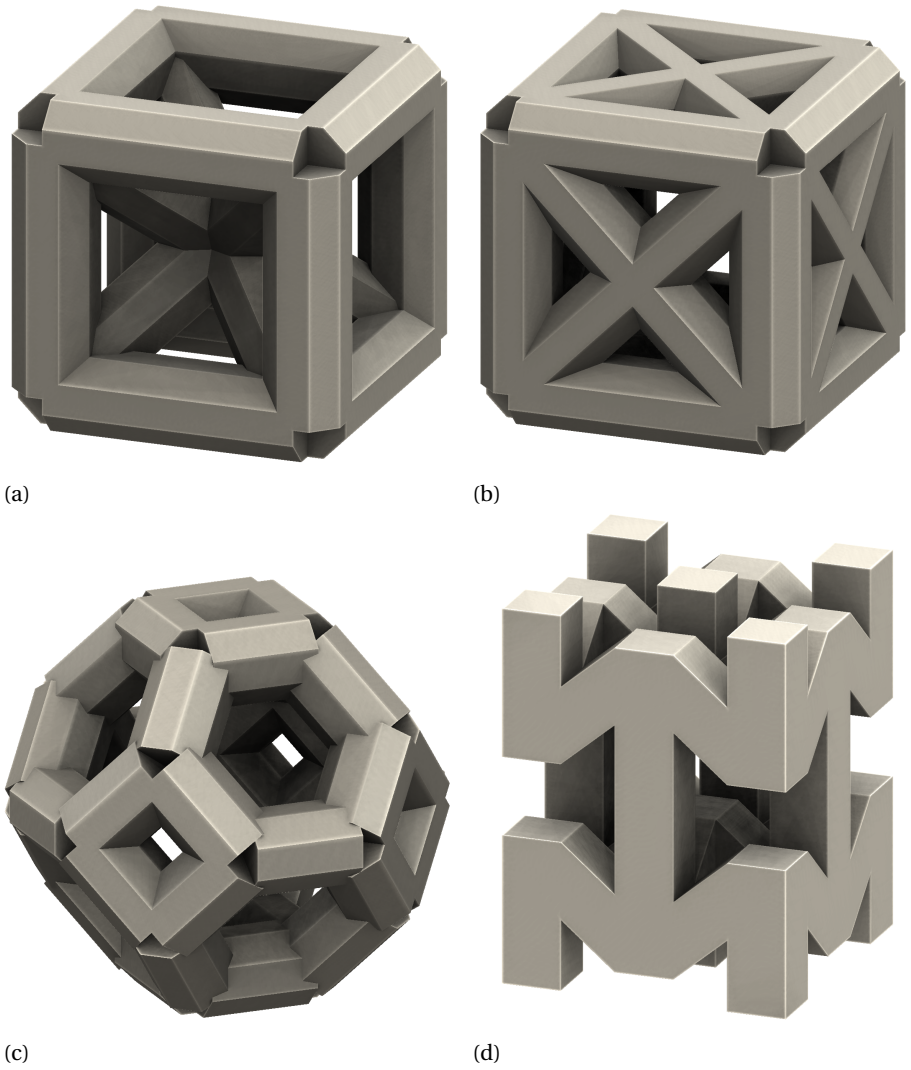

Figure 2.2: CAD models of unit cell designs: a) Body Centered Cube (BC-cube), b) Face Centered Cube (FX-cube), c) Truncated Octahedron (T-octa), d) Negative Poisson's Cube (NP-cube).

The scaffold height ranged from 5.5 to 12.3 mm, depending on the unit cell and porosity. This was in the range of the human IVD height [13], and although there is a noticeable difference in height between the designs, this was done to maintain the same pattern. The nominal cross section ranged from 169 to 475.2 mm^2, again depending on the unit cell and porosity. The base was printed with 100% infill, with the stiffness of the base kept higher than that of the lattice structure in between.
The porosity was determined for all scaffolds as follows:

$$P = 1 - \frac{Volume_{scaffold}}{Volume_{solid}}$$

Where $Volume_{scaffold}$ is the total volume of the 5x5x2 scaffold and $Volume_{solid}$ is the volume if the outer dimensions of the scaffold would form a solid box. Individual unit cells have a slightly different porosity than

Table 2.1: Number of samples.

Unit cell	BC-cube			FX-cube			T-octa			NP-cube		
Porosity[%]	$50_{\parallel}$	$50_{\perp}$	$70_{\perp}$	$50_{\parallel}$	$50_{\perp}$	$70_{\perp}$	$50_{\parallel}$	$50_{\perp}$	$70_{\perp}$	$50_{\parallel}$	$50_{\perp}$	$70_{\perp}$
Number of samples	3	3	3	3	3	3	3	3	3	3	3	3

whole scaffolds, because individual cells in scaffolds have the same adjacent truss.
The truss thickness was kept constant at 0.8mm, while the porosity and 3D printing direction were variables. The 3D printing direction was either parallel (called parallel $\parallel$) or perpendicular (called perpendicular $\perp$) to the direction of testing.
For the first test cycle, a porosity of P=50% and both printing directions were chosen. In order to assess the effect of considerable changes in porosity, a second cycle was introduced with P=70% for the BC-cube, FX-cube and, T-cube and the NP-cube printed at a perpendicular 3D printing direction, which showed better mechanical properties. Table 2.1 shows the number of printed samples to be characterised and tested later on.
The pore size was not user-defined, as the truss diameter and porosity were already used as boundary conditions, therefore pore size was not a concern for this research.

The BC-cube (Figure 2.2a) and the FX-cube (Figure 2.2b), both from the cubic family, have an octagonal cross section, as was the case in the studies by Egan [49]. A BC-cube has trusses at the edges of the cube and additional beams extending from the corners to the center of the cube. It has been shown to be advantageous because it maintains high porosity, shear modulus and surface-to-volume ratio compared to other topologies [49].
The FX-cube has trusses at the edges of the cube and includes beams from corner to corner on each face of the cube. It showed good Elastic modulus values at useful porosity for tissue ingrowth [48], and the nominal scaffold size was still not too large at the selected porosity because the interior of the cell was free of beams.

The T-octa unit cell (Figure 2.2b), from the Truncated Family, has also an octagonal cross section. The T-octa cell is created by taking an octa cell (with beams that begin and end in the center of each cubic volume face) and putting it in a square shape for each octa cell connection [49]. This unit cell was of interest because Egan described that although the T-octa cell has a relatively low modulus of elasticity compared to other unit cells tested, he attributed this to a bending dominated topology of the cube [49], and believed that this would be well-suited for applications where energy absorption is advantageous.

An orthotropic 3D re-entrant auxetic structure was selected as the unit cell that displays negative Poisson's ratio. The design parameters of the NP-cube is based on the paper of Yang et al. [55], where the design goes from a 2D (Figure 2.3a) to a 3D (Figure 2.2d) re-entrant lattice structure. The Poisson's ratio and porosity were defined through an iterative procedure of tuning the geometry, such that the nominal scaffold size would be in the range of other scaffolds for the 5x5x2 pattern. A square cross section was used for the trusses, so that the properties could be calculated as described by Yang et al. [55]. A Matlab script was written to tune the design with the geometry parameters as input and Poisson's ratio as output, using the equation $\nu = \frac{L^2 cos\theta(\alpha - cos\theta)}{2\alpha t^2 + L^2 sin^2\theta}$. The parameters in the equation are visible in Figure 2.3b and where t is the truss thickness and $\alpha = H/L$. Once the geometry parameters were known, the design was drawn in Solidworks to obtain a unit cell. This cell was then patterned to achieve the desired scaffold of 5x5x2 unit cells. Then the porosity was calculated from the known volume of the scaffold from Solidworks and the calculated solid volume. If the desired porosity was not yet achieved, the procedure was repeated until the desired porosity was reached. The Poisson's ratio, which was found to work well after iteration, was ν=-0.71 and was kept constant for 50% and 70% porosity.

2.2. 3D printing

For the production of the lattice structures an Objet500 Connex3 (Stratasys, USA) was used. It utilizes polyjet 3D printing which is a technique where the print head jets microscopic layers of liquid photopolymer onto a build tray and instantly cures it with UV light [66]. This process is repeated until all layers make up the desired part. The layer resolution was set to 30-micron. A photopolymer material VeroWhitePlus (Stratasys, USA) was used (ρ = 1.17–1.18g/cm^3, $E = 2000-3000MPa$, $T_g = 52-54°$). This material has identical mechanical properties as the bio-compatible MED610 polymer which was used in the study of Egan [67], allowing to

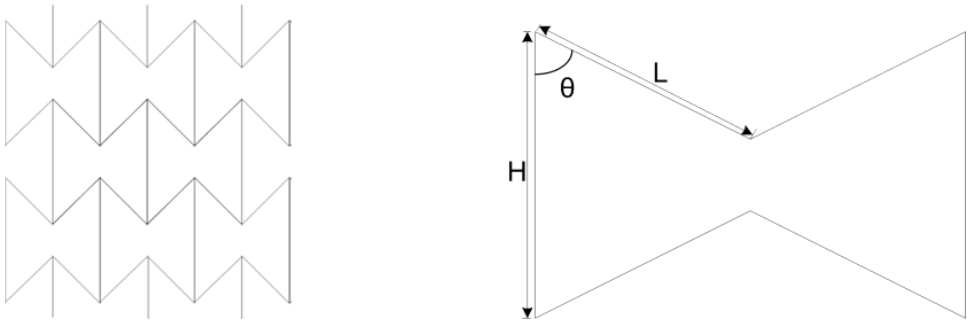

(a) (b)

Figure 2.3: a) 2D re-entrant auxetic unit cell. b) Parameters that define the re-entrant auxetic unit cell. [55]

compare the results. However, VeroWhitePlus is not biocompatible, but this was not an issue in this study as no biological tests were involved.
The samples were printed in combination with SUP706 support material, which filled the voids and surrounded the samples (Figure 2.4a). The support material was removed by immersing the printed parts in a base solution of 2% NaOH:1% Na_2SiO_3 in distilled water, and stirring them with a magnet for 7-10 hours (Figure 2.4b). The samples were later rinsed with water, immersed in 5% acetic acid solution for one minute, rinsed with water again and dried in the air (Figure 2.4c).

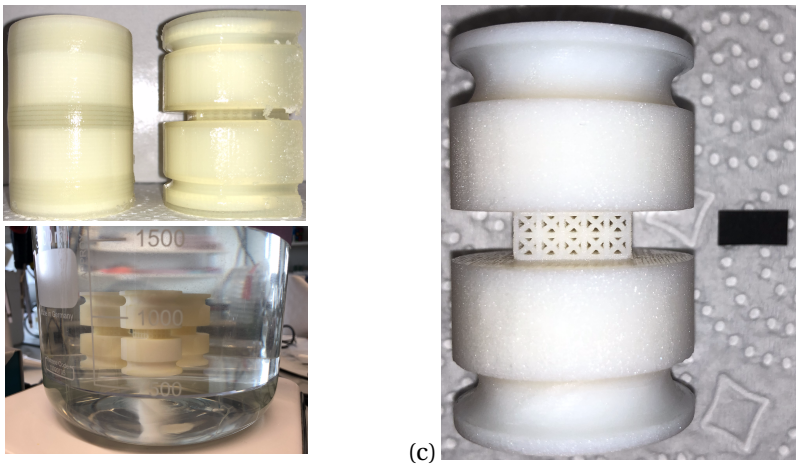

(a) (b) (c)

Figure 2.4: a) Samples after 3D printing in different directions, left: parallel, right: perpendicular. b) The support material dissolved in a base solution while a magnet stirring underneath the samples. c) Sample after the cleaning process.

The density and elastic modulus of the nominal material were determined by 3D printing 6x6x6mm solid cubes. The density was determined $\rho = 1.13 g/cm^3$, and the modulus of elasticity $E = 1940 MPa$.
The samples were weighed (Mettler Toledo, USA) and the nominal height and cross-section were measured using a caliper (Mitutoyo, Japan). Using a Dino-Lite digital microscope, images were taken with an object of known scale to see the 3D printing imperfections and to determine the beam diameter. The beam diameters were measured from the images using ImageJ software. The plots for the nominal dimensions and beam diameters were done using GraphPad Prism v8.0.
A micro-CT (Scanco Medical μCT100, Switzerland) at medium resolution (80μm voxel size) was employed to image one sample from each group and compare the 3D printed parts to the CAD model. The image analysis was performed in MITK-GEM 2016.

2.3. Embedding of Samples

Since the dynamic mechanical experimental testing setup originated from earlier studies by Marini [24], it was necessary to embed the 3D printed samples in the metal cups to be able to carry out the experiment. This process was very slow, as the samples were brittle and could break easily, while at the same time a very

careful attention was paid to embedding the samples perpendicular to the bottom cup face using a spirit level.

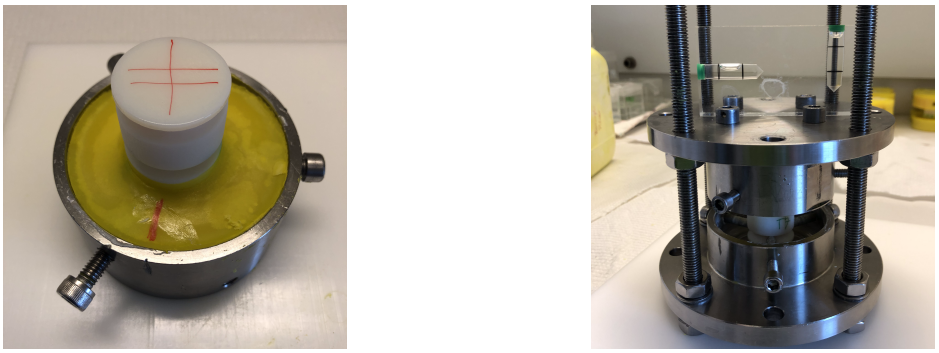

(a) (b)

Figure 2.5: a) First embedding of the sample in the top cup. b) Second embedding of the sample in the bottom cup.

The base of the sample was held in place with three screws fastened into the U-notch and surrounded by a 2-component acrylic system for embedding for grinding in material testing (Suter Kunststoffe AG) in a volume ratio: powder (SCS-Beracryl D 28 Powder):liquid (SCS-Beracryl D 28 Liquid) = 100:50 (Figure 2.5a). The cups were coated with moisturizing cream, which facilitated the removing of the samples. The samples were first embedded in the top cup (Figure 2.5a), left to harden for about 30 minutes. Then the samples were reversed and mounted on an embedding assembly of four rods connected to the bottom cup (Figure 2.5b) and embedded. After hardening of the samples, they were carefully removed from both cups, inspected, labeled and stored.

2.4. Mechanical testing

Static compression and dynamic tests were performed on Instron E10000 ElectroPuls™in air and at room temperature.

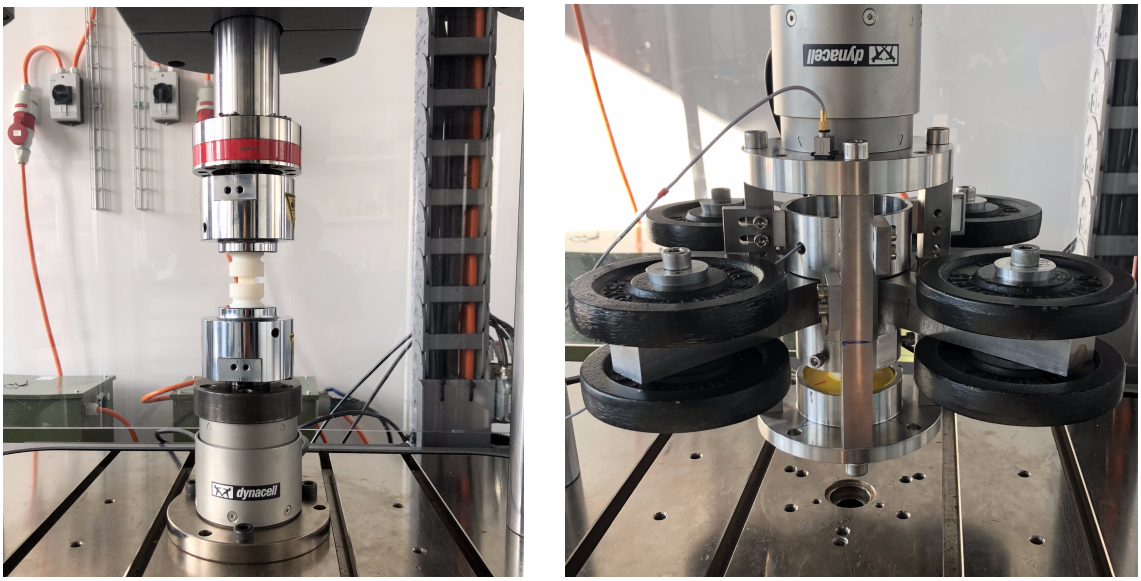

(a) (b)

Figure 2.6: a) Static testing setup on Instron. b) Dynamic testing setup on Instron.

2.4.1. Quasi-Static compression test

Quasi-static compression tests were carried out before the dynamic test and embedding of samples. The samples were placed between two flat compression platens (Figure 2.6a) and a 10kN load cell measured the force. The compression tests were performed in displacement control. The compression speed rate was determined based on tests on similar scaffolds from Egan [48], where the rate was defined as 20% strain (of the scaffold height) in 1 minute of loading. Since the samples had to be undamaged after the compression test in order for the dynamic test to be performed, the compression was conducted to a maximum of 3% strain (of the scaffold height). Matlab was used to interpret the Instron data and determine, in the linear region of the force-displacement curve, the elastic modulus E and stiffness k (Appendix E). Where necessary, the measured sample dimensions were used for the calculations. Four compression tests were performed for each sample and the last three were taken to calculate the mean value and standard deviation. Stress-strain of all unit cell types, 3D-printing directions and porosity were done using Matlab.

2.4.2. Dynamic test

After the quasi-static test had been performed, the samples were embedded in the test cups (as described in section 2.3) and mounted in the test setup (as shown in Figure 2.7d).
A test fixture, which was already applied to test a human functional spine unit (FSU) [24], was used (Figure 2.6b). It mimics a base excitation model (Figure 2.7b), in which the top free moving mass represents the upper body weight pressing on the specimen while a cyclic displacement was applied to the sample from below. The upper mass consisted of the four-arm crossbar bolted to the top embedding cup and restraining cylinder which combined for 6kg. Additional weights of 1.25kg each could be added on each end of the four-arm crossbar, which were fixated by using conical designed holders (Appendix C). Marini showed that the crossbar's structure has the first mode of oscillation above 210Hz [24] and would not interfere with the testing results.
A new adapter plate between the Instron and the testing setup had to be designed and manufactured (Appendix A), as the mechanical test device in the previous work (MTS Bionix®, USA) was different from the current one (E10000 ElectroPuls™, Instron®, USA). The bottom cup (Appendix B) was redesigned and newly manufactured. The Instron actuator transferred the vertical movement to the bottom embedding cup via an adapter plate and four pillars (Figure 2.7a-d). To prevent the upper mass from moving perpendicularly to the direction of excitation, a restraining cylinder was limited by eight low-friction Teflon holders, which were regularly lubricated with a silicone lubricant.
The accelerations were recorded by two accelerometers (4508 B 004, Brüel & Kjaer, Nærum, Denmark), one ($\ddot{x}$) on the top of the crossbar on the center of the free moving top (see Figure 2.7d) and the second ($\ddot{y}$) on the adapter plate (see Figure 2.6b, 2.7a,c). The accelerometer $\ddot{y}$ measured the input from the bottom of the sample, but was placed on the adapter plate. This was done to protect the sensor from constant assembly and disassembly for each sample after it had been determined that the location of the sensor has a negligible effect on the signal. The accelerometers were connected to a conditioning amplifier (2693-A-0S4, Brüel & Kjaer, Nærum, Denmark) which in turn was connected to a DAQ (myDAQ University Kit, National Instruments, USA). The program was written in LabVIEW (National Instruments, USA) (Appendix 4) to control data capturing (time, both accelerations) and save the data in a text file for later data analysis. The sample rate was set to 10kHz.

The dynamic test methodology was based on the Marini study [24]. After carefully mounting the sample in the bottom cup, the Instron was lowered so that the four pillars and the crossbar with the top cup slid onto the top part of the sample. After carefully tightening the screws into the cups, the Teflon holders were inspected and tightened if necessary. A constant sinusoidal displacement to the lower embedding cup was applied and controlled through the Instron by the user. The function that was exciting the sample from the bottom was in the form of:

$$y = y_0 sin(2\pi f(t)t)$$

and had a frequency sweep rate of $0.1Hz/s$ while the y_0 amplitude was set to 0.1mm for all samples. The frequency increased linearly from a set low frequency $10Hz$ to a set high frequency $60Hz$ (Increasing Frequency Sweep, IFS), and if the sample did not break, the frequency was reversed (Decreased Frequency Sweep, DFS) back down to $10Hz$. The broad frequency range was in the scope where dangerous effects on the IVD were observed [24, 27, 33] and increased to a maximum of $60Hz$, where it was still comfortable and safe to use the Instorn testing device. The mass on top of the sample was 16kg, of which 10kg was from the eight added weights and 6kg from the crossbar, restraining cylinder, top cup and some bolts. The preload was chosen

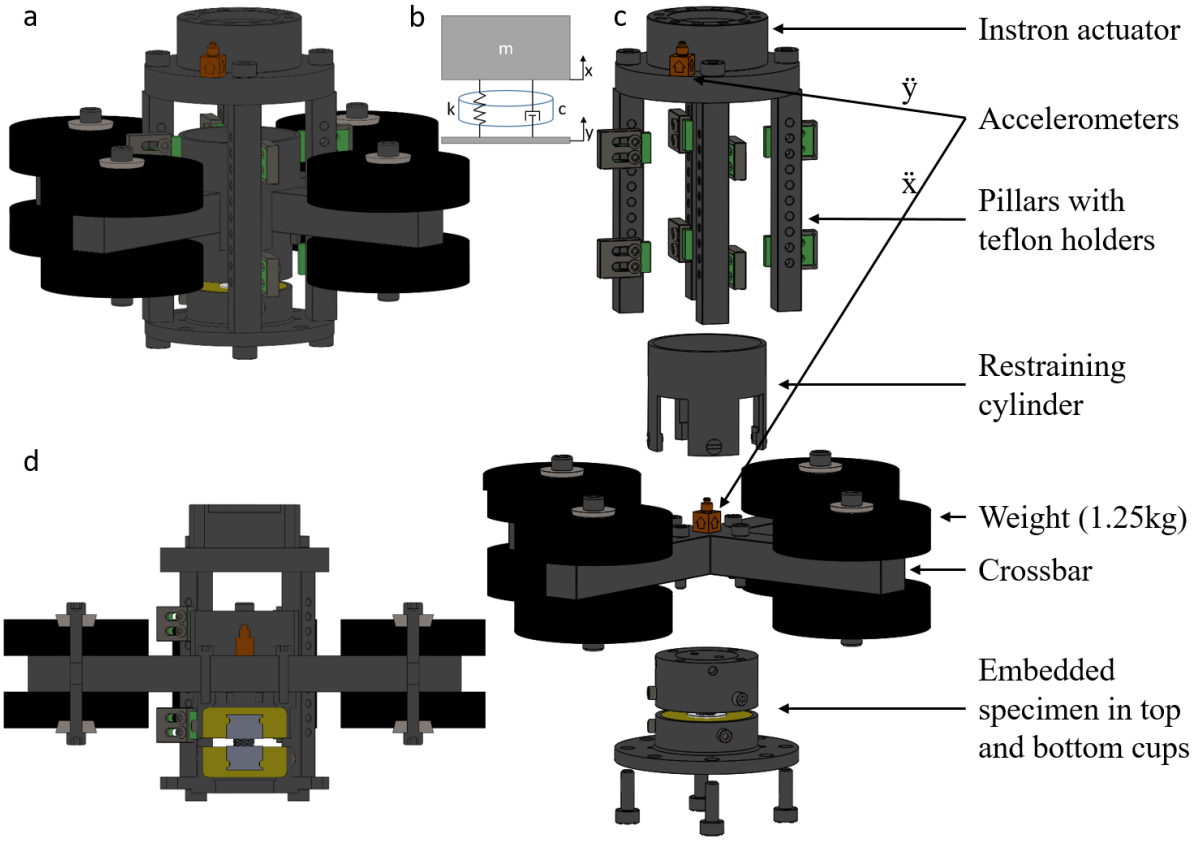

Figure 2.7: a) Dynamic testing setup. b) Base excitation model depicting what the dynamic testing setup is trying to resemble. c) Exploded view of the dynamic setup . d) Cross section of the dynamic setup.

based on the minimal weight that Marini used on human IVD testing and more weight was not added, for the safety of the testing device and the surroundings. If the sample broke, the test and data acquisition was stopped, otherwise the samples were carefully removed and stored.
The collected accelerometer data was imported into Matlab (Appendix F). Before the data was evaluated, a low-pass Butterworth filter (passband frequency 75Hz, stopband frequency 120Hz, passband ripple 0.1dB, stopband attenuation 200dB) was applied to the signal, to filter out any noise. After filtering the signal, a Fourier transform was utilized to change the data from time domain to frequency domain. To assess the magnitude of the response of the top free moving mass signal $\ddot{x}$ to the input signal $\ddot{y}$, the ratio response to input was computed, known as the transmissibility function $T(\omega) = \ddot{X}(\omega)/\ddot{Y}(\omega)$. The Fourier transforms were used for the calculations, which show the response of the system with respect to the specific frequency. Gain and phase were observed and using the transmissibility function, the peak values of the $T(\omega)$ were determined at the frequency of sample failure. If the sample did not fail, the peak $T(\omega)$ value was determined and the differences between the IFS and DFS were observed.

2.5. Statistical analysis

Statistical analysis was done in GraphPad Prism v8.0. When comparing the measured scaffold length and height a unpaired t test with Welch's correction was used for the statistical analysis.
A Multiple comparisons ordinary one-way Anova statistical analysis was done on Elastic modulus results from the compression test comparing different unit cell types. To compare the change of Elastic modulus withing a unit cell type group, while changing either the 3D-printing direction or the porosity from 50% to 70%, a unpaired t test with Welch's correction was used for the statistical analysis.

3
Results

3.1. Build accuracy

Samples with fixed beam diameter ϕ=0.8mm and 5x5x2 unit cell pattern with changing unit cell type, porosity and 3D-printing direction were manufactured. The samples were difficult to work with and required meticulous handling not to get damaged and/or broken, especially when a heavy mounting testing setup was used.

In Table 3.1, the nominal dimensions of the lattice design and mean measurements with standard deviation of the manufactured samples are displayed. The mean nominal scaffold length dimensions were generally accurate with 1.7% being the biggest difference while the mean nominal height dimensions were slightly less accurate with 9.6% being the biggest difference between the measured and the designed values. The scaffolds measured length was within 0.23mm while their height was within 0.53mm of their designed dimensions. The length of all printed scaffolds does not have a large deviation from its design dimension, and with a small bias of being too large for the P=50%$_{\parallel}$ whereas the length of other scaffolds do not show a consistent deviation (Figure 3.1a-d). The 3D printing direction (for P=50 % both the $\parallel$ and $\perp$) seems to have a slight influence on the scaffold length since for all unit cells the parallel samples have a larger scaffold length for all unit cells, but does not show significance for any unit cell type. The p-values when comparing P=50$_{\parallel}$ and 50$_{\perp}$ are 0.0657 for the BC, 0.1256 for the FX, 0.3530 for the T and 0.3155 for the NP-unit cell. The scaffold height measured between the bases was in most samples smaller than the CAD design. The deviation was within 1% of the CAD height, except for the parallel 3D-printed unit cells, which showed a larger deviation of the designed height (Figure 3.1e-h). For the BC unit cell P=50% scaffolds, both the parallel and perpendicular 3D-printing direction, had a noticeable higher scaffold height than the designed dimension (Figure 3.1e). The 3D-printing direction for all unit cells (for P=50% $\parallel$ and $\perp$) shows that when printed in a perpendicular direction, the samples are higher. The influence of 3D-printing direction on height was significant for all unit cell types(Figure 3.1e-h). The weight of the whole scaffolds represents the weight of the scaffold and its two

Table 3.1: Nominal design values compared to the measurements after fabrication. All scaffolds had a 5x5x2 unit cell configuration. Sample measurements are presented as Mean (SD).

	Lattice design						Mean measurements		
Unit cell	Porosity [%]	Diameter [mm]	Unit cell length [mm]	Length [mm]	Height [mm]	Weight of whole sample [g]	Length [mm]	Height [mm]	Weight of whole sample [g]
BC	50$_{\parallel}$	0.8	2.6	13.80	5.50	29.84	14.03 (0.09)	5.9 (0.02)	30.78 (0.06)
	50$_{\perp}$	0.8	2.6	13.80	5.50	29.84	13.79 (0.13)	6.03 (0.03)	30.49 (0.35)
	70$_{\perp}$	0.8	3.6	18.80	8.00	30.20	18.77 (0.09)	7.95 (0.02)	30.82 (0.03)
FX	50$_{\parallel}$	0.8	2.8	14.80	6.40	30.07	15.00 (0.13)	6.12 (0.02)	31.28 (0.05)
	50$_{\perp}$	0.8	2.8	14.80	6.40	30.07	14.82 (0.05)	6.43 (0.01)	30.89 (0.08)
	70$_{\perp}$	0.8	4.2	21.80	9.20	30.75	21.82 (0.13)	9.15 (0.02)	31.40 (0.03)
T	50$_{\parallel}$	0.8	2.4	13.00	5.70	29.67	13.10 (0.13)	5.38 (0.03)	30.86 (0.02)
	50$_{\perp}$	0.8	2.4	13.00	5.70	29.67	13.01 (0.02)	5.65 (0.02)	30.42 (0.05)
	70$_{\perp}$	0.8	3.2	16.80	7.20	29.89	16.75 (0.04)	7.12 (0.02)	30.48 (0.02)
NP	50$_{\parallel}$	0.8	3.9	16.30	10.10	31.38	16.27 (0.17)	9.89 (0.05)	31.39 (0.03)
	50$_{\perp}$	0.8	3.9	16.30	10.10	31.38	16.14 (0.03)	10.09 (0.02)	31.20 (0.08)
	70$_{\perp}$	0.8	4.6	19.65	12.30	31.90	19.67 (0.06)	12.22 (0.02)	31.29 (0.01)

bases. Since the bases are considerably heavier than the scaffolds, and the latter contribute only around 2%

of the total weight, it is not possible to determine any changes of mass between 3D printing directions just for the scaffolds. It is, however, possible to say, that in general the 3D-printed samples were heavier than the designed parts (ranging up to 4%). Only the perpendicular NP unit cell samples showed a slightly smaller mass (up to 2.1% smaller for the NP70$_\perp$) compared to the designed weight, while for the parallel NP scaffold the difference was negligible.

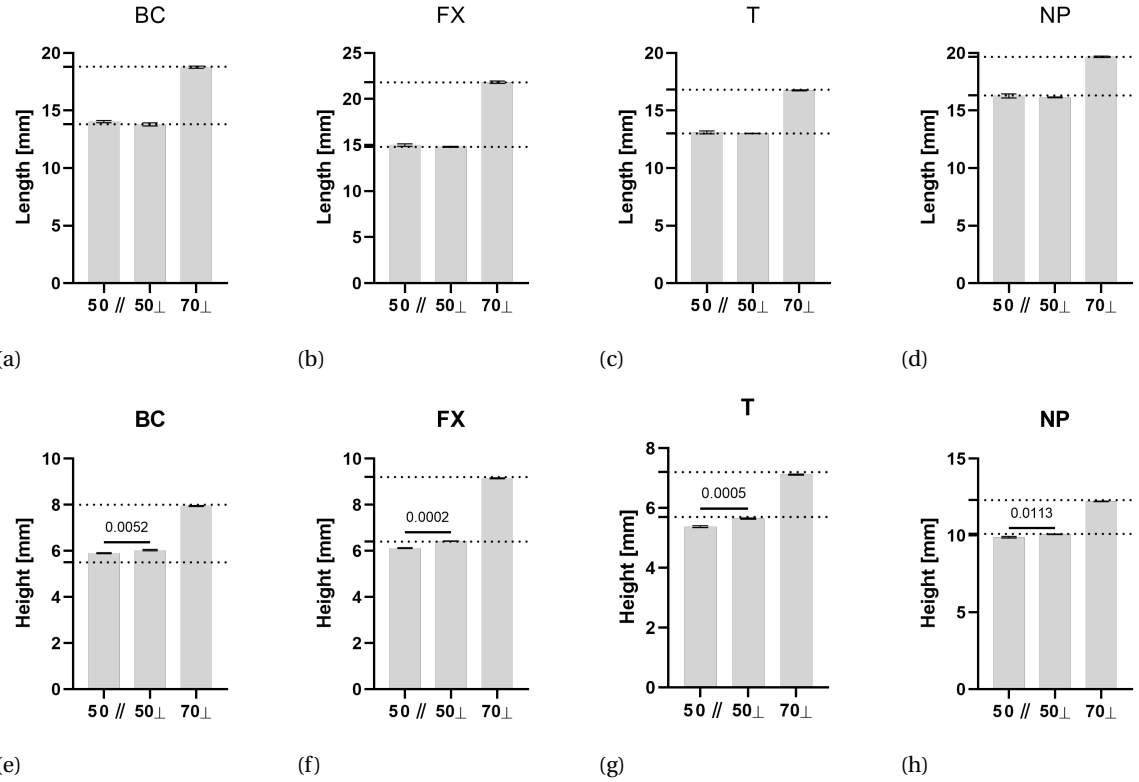

Figure 3.1: Measured scaffold length and height for all 3D-printed unit cells (columns) and their corresponding CAD values (dotted lines). On all plots, the x-axis represents porosity in % and the 3D-printing direction.

Beam diameter

Observation of the influence of 3D-printing direction, unit cell type and porosity on beam diameter and print quality in general was done using a digital microscope. The 3D-printing direction (Figure 3.2a) determines how the layers are stacked upon each other. Regarding parallel printing direction, all sides of the scaffold are the same (in Figure 3.2a S1=S2). Perpendicular direction on the other hand exhibits some differences between the side that was parallel to the printing bed (S2) and the side that was perpendicular to the printing direction (S1). Thus, in case of the parallel 3D-printing direction samples beam measurements for the S1 side are given, while for the perpendicular 3D-printing direction, measurements for S1 and S2 were taken.
The visual difference between printing direction, when observing the same unit cell type (BC) and porosity(P=50%), are clearly seen in Figure 3.3. The layers are distinguishable and the S2 side of the perpendicular sample has a visual different appearance, since it is either the first or the last building layer of the scaffold. In Figure 3.3c, an error in the finished part is enlarged and this was just one of many that we have observed.
In Figure3.4, figures of all unit cell types, 3D-printing direction and porosity are shown. Next to the visible change in 3D-printing direction previously described, the change of porosity within a unit cell type clearly shows a higher quantity of empty volume space, desirable for better fluid flow. In the T unit cell type, some design features were melted together with others, when compared to the CAD model. This is due to the fact that the design features were so small and the 3D-printing technique not accurate enough, hence some details have been lost.

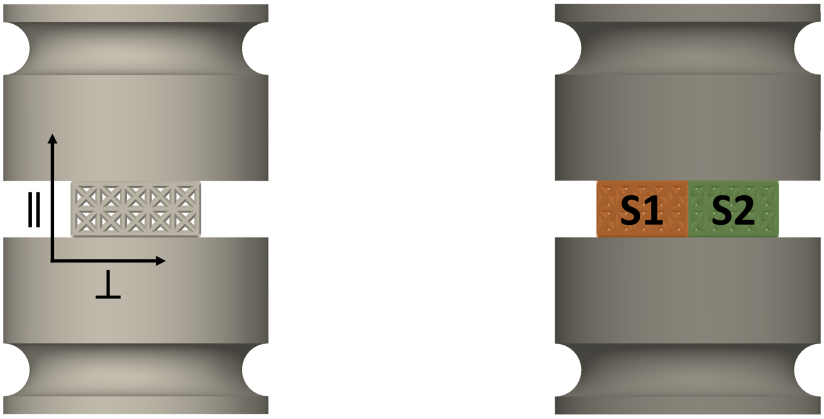

(a) (b)

Figure 3.2: a) Printing directions, ∥-parallel and ⊥-perpendicular. b) Scaffold sides, S1 and S2.

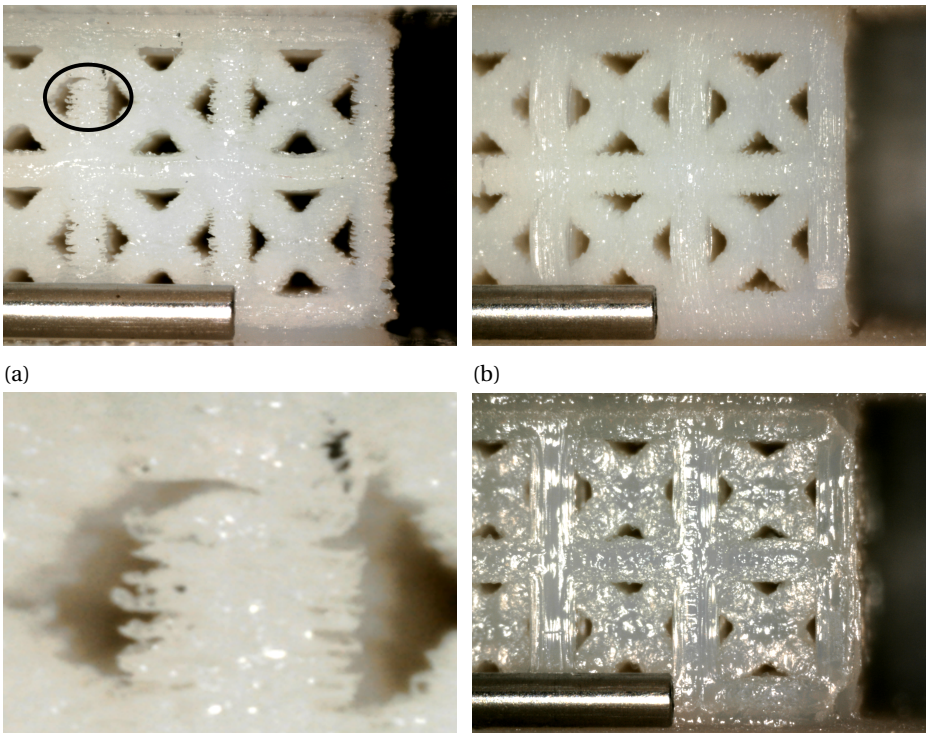

(a) (b)

(c) (d)

Figure 3.3: Figures of BC cube of 50% porosity: a) parallel printing, S1 side, b) perpendicular printing, S1 side, c) Enlarged error in 3D printing from parallel printing (Figure 3.3a), d) perpendicular printing, S2 side. The width of the metal object in the bottom left is 1mm.

In the described sides of the scaffold (S1 and S2), the beams were grouped in 3 directions of the beam orientation. 0deg was defined as the the beams being parallel with the testing direction, 90deg beams as being perpendicular to the testing direction, while 45deg beams are aligned between the 0deg and 90deg beams. For perpendicular printed samples samples on the S2 side, the 0deg and 90deg beams were grouped together because the 3D printing did not have an effect on the beam build quality. For the NP unit cell scaffolds, there are no 90deg beams and therefore these measurements are absent in S1 and S2 sides.

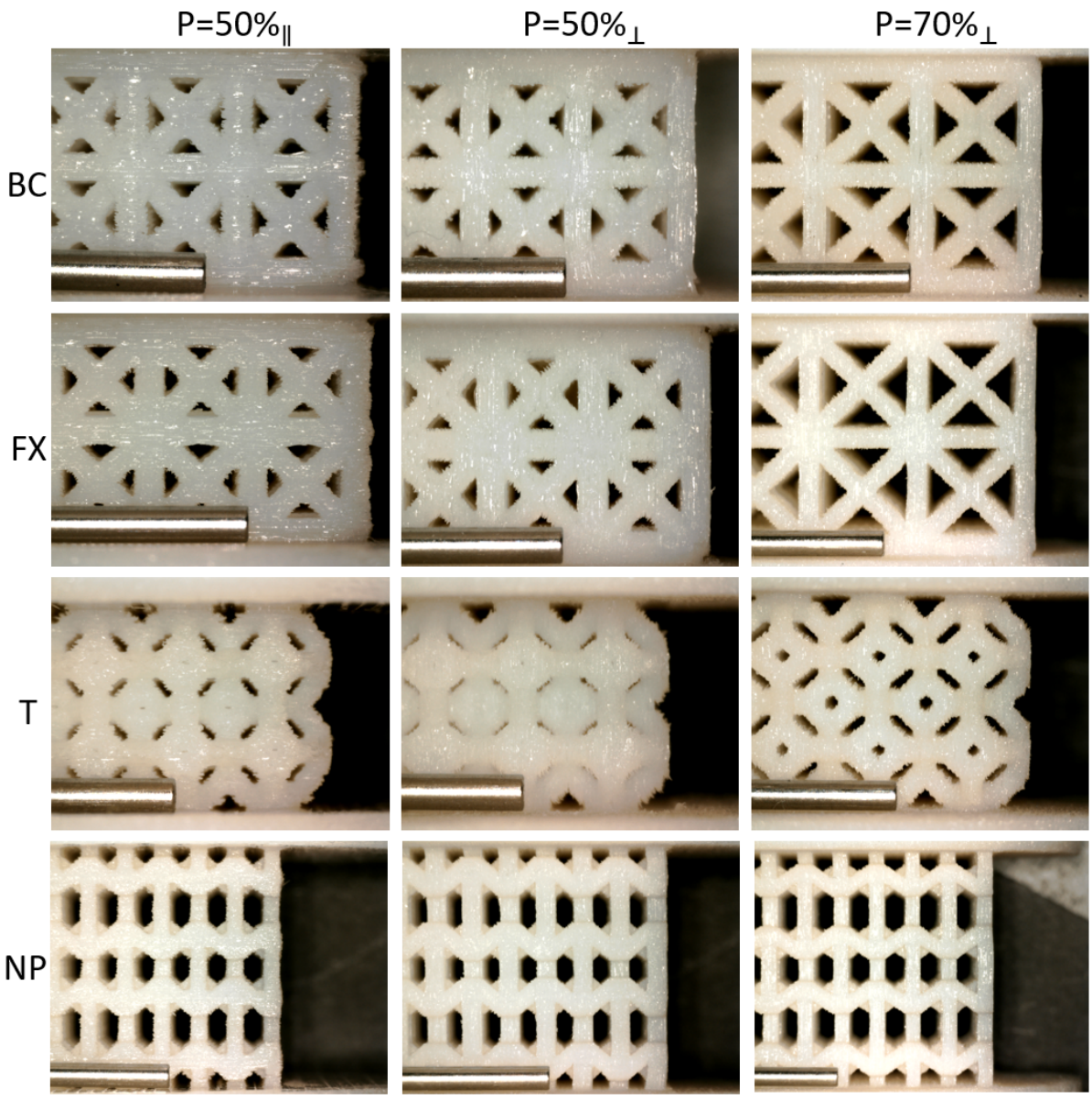

Figure 3.4: The scale (the width of the metal object in the bottom left) is 1mm.

Table 3.2: Mean beam diameter with standard deviation (SD) for all unit cell types, porosity and printing direction. Maximum and minimum local beam diameter measurements on the right.

Lattice design			Side S1			Side S2		Local beam diameter		
Unit Cell	P [%]	Diameter [mm]	0 deg [mm]	45 deg [mm]	90 deg [mm]	0/90 deg [mm]	45 deg [mm]	min [mm]	max [mm]	range [mm]
BC	$50_{\parallel}$	0.800	0.778 (0.020)	0.744 (0.025)	0.682 (0.029)	/	/	0.655	0.797	0.142
	$50_{\perp}$	0.800	0.749 (0.014)	0.737 (0.019)	0.743 (0.016)	0.819 (0.034)	0.805 (0.017)	0.692	0.873	0.181
	$70_{\perp}$	0.800	0.796 (0.028)	0.845 (0.023)	0.831 (0.021)	0.881 (0.019)	0.842 (0.015)	0.759	0.918	0.159
FX	$50_{\parallel}$	0.800	0.820 (0.023)	0.740 (0.018)	0.787 (0.022)	/	/	0.705	0.861	0.156
	$50_{\perp}$	0.800	0.817 (0.025)	0.762 (0.021)	0.884 (0.015)	0.832 (0.048)	0.789 (0.028)	0.740	0.905	0.165
	$70_{\perp}$	0.800	0.782 (0.011)	0.840 (0.017)	0.821 (0.018)	0.862 (0.026)	0.880 (0.022)	0.766	0.920	0.154
T	$50_{\parallel}$	0.800	0.743 (0.020)	0.699 (0.038)	0.751 (0.025)	/	/	0.645	0.788	0.143
	$50_{\perp}$	0.800	0.796 (0.023)	0.779 (0.036)	0.791 (0.041)	0.839 (0.029)	0.786 (0.021)	0.733	0.894	0.161
	$70_{\perp}$	0.800	0.798 (0.019)	0.804 (0.030)	0.885 (0.021)	0.909 (0.028)	0.857 (0.027)	0.751	0.966	0.215
NP	$50_{\parallel}$	0.800	0.717 (0.028)	0.728 (0.028)	/	/	/	0.676	0.769	0.093
	$50_{\perp}$	0.800	0.791 (0.020)	0.760 (0.022)	/	0.844 (0.027)	0.829 (0.029)	0.725	0.887	0.162
	$70_{\perp}$	0.800	0.801 (0.015)	0.809 (0.019)	/	0.932 (0.021)	0.908 (0.014)	0.776	0.969	0.193

In Table 3.2, the mean beam diameter measurements with the standard deviation are included all unit cells. It also contains the minimum, the maximum and the range for the local beam diameter, which includes all beam orientations in the given sample.
The designed beam diameter was set at 0.800mm while the measured local beams ranged from 0.645mm ($T50_{\parallel}$) to 0.969mm($NP70_{\perp}$). The range width varied from 0.093 for $NP70_{\parallel}$ to 0.215mm for $T70_{\parallel}$. The standard deviation of beam measurements ranged from 0.011 to 0.048 which shows that there were small deviances within a beam orientation for each sample.
In general, $50_{\parallel}$ samples had lower than the designed beam diameters, whereas the rest, for side S1, varied from being undersized to being oversized. The S2 side, however, shows that there is a trend that most beam diameters are larger than the CAD 0.800mm diameter.
In Figure 3.5a the mean beam measurements with the standard deviation for the S1 side are provided for all unit cell types, 3D-printing direction and porosity. Side S2 is graphically presented in Figure 3.5b as mean values with the given SD. However, for side S2 the 0deg and 90deg values are combined (NP has only 0deg measurements).

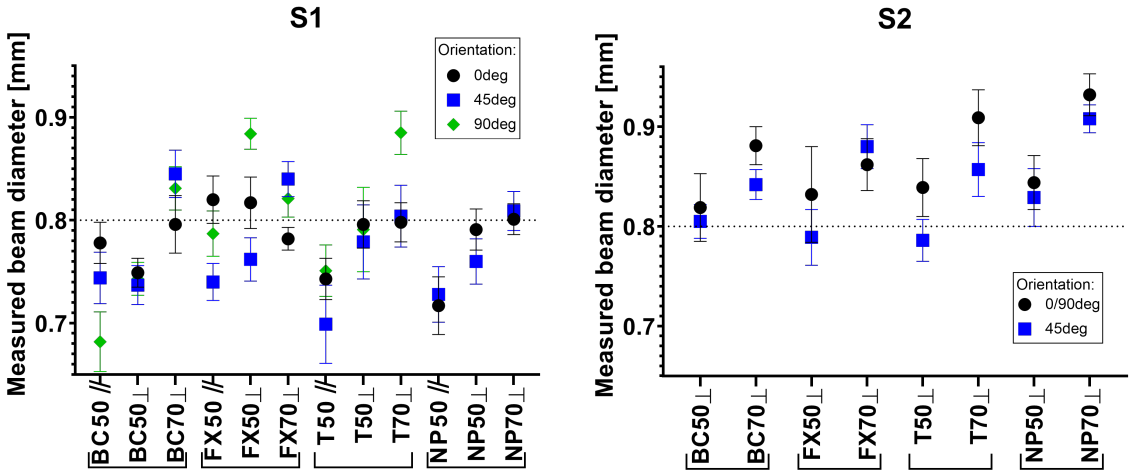

(a) (b)

Figure 3.5: Beam diameter measurements for: a) side S1, b) side S2. The dotted line represents the desired design beam diameter.

Micro CT

Micro CT scanning was performed on selected samples to determine the volume of the manufactured parts (V_{CT}) and to compare them to the designed CAD volume(V_{CAD}). The volumes of CAD compared to the CT values can be observed in Table 3.3.

First, three samples per group for $BC50_{\parallel}$ (Figure 3.6b), $BC50_{\perp}$ and $BC50_{\parallel}$-just scaffold (Figure 3.6a) were scanned and the mean values with standard deviation were determined. The rest of the unit cell types had one sample per group. The just scaffold volume was compared to the scaffold whose top and bottom base were removed in software post processing from the micro-CT model. This comparison was made to see the effect of 3D-printing a base on top and bottom of the scaffold. Comparison between 3D-printing directions, while keeping the unit cell type and porosity unchanged, was made between $BC50_{\parallel}$ and $BC50_{\perp}$. For all samples whose standard deviation was determined, this was low for all groups, reaching up to 1.2mm^3 for the BC just scaffold. This indicated that there was not much deviation within a sample group. Volume of printed samples was also determined for the 70% porosity samples, to check how the change of porosity may influence the volume difference from the CAD models (Figure 3.6c).

All measurements show that the sample volume is lower than the designed volume. This ranged from -10.4% lower for the $FX50_{\perp}$ and 29.0% lower for the $NP50_{\parallel}$. The $BC50_{\perp}$-just scaffold was 17.2% smaller compared to the CAD while the cut $BC50_{\perp}$ was 22.5% smaller. The $BC50_{\parallel}$ was 23.9% smaller compared to CAD. The 3D-printing direction shows that for all unit cell types the parallel direction has a noticeable smaller volume than that of the perpendicular. 70% porosity causes the volume to become smaller again which is true for all unit cell types at around 20% smaller for all groups.

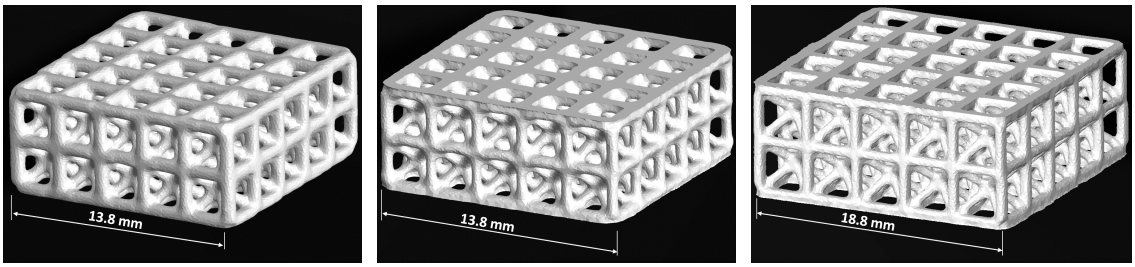

(a) (b) (c)

Figure 3.6: μCT imaging of BC cube perpendicular 3D printing direction: a) 50% porosity scaffold only, b) 50% porosity scaffold with a removed top and bottom base, c) 70% porosity scaffold with a removed top and bottom base.

Table 3.3: Scaffold volume of CAD model compared to measured Volume from CT imaging.

	BC just scaffold	BC			FX			T			NP		
P[%]	$50_{\perp}$	$50_{\parallel}$	$50_{\perp}$	$70_{\perp}$	$50_{\parallel}$	$50_{\perp}$	$70_{\perp}$	$50_{\parallel}$	$50_{\perp}$	$70_{\perp}$	$50_{\parallel}$	$50_{\perp}$	$70_{\perp}$
V_{CAD}[mm^3]	568.5	568.5	568.5	885.74	778.4	778.4	1374.9	418.0	418.0	614.6	1186.4	1186.4	1489.8
V_{CT}[mm^3]	470.9 (1.2)	432.5 (1.3)	440.8 (0.7)	666.0	613.5	697.4	1116.3	353.4	368.8	490.8	842.8	945.5	1160.5
Change [%]:	-17.2	-23.9	-22.5	-24.8	-21.2	-10.4	-18.8	-15.4	-11.8	-20.1	-29.0	-20.3	-22.1

3.2. Compression test

Compression test was carried out on 3 samples per each group. The mean elastic modulus with their corresponding standard deviations and the sample stiffness were calculated from the Instron data collected (Table 3.4). For every sample 3 compression tests were conducted, and all samples had very little deviation, ranging from less than 0.1% up to 3% from their mean calculated values. This indicated that the testing method and the testing setup were adequate. The deviation within groups was higher, indicating that the 3D-printing of the samples does not always produce the same quality parts. For most groups, the standard deviation was within 5% of the mean calculated elastic measurements, while for BC50 parallel and perpendicular groups the deviation was higher. The $BC50_{\parallel}$ sample exhibited as much as 20.4 MPa (14%) and $BC50_{\perp}$ samples 43.4 MPa (23.3%).

All samples were compressed to 3% of their scaffold height, except for $NP70_{\perp}$ where the strain was applied to 2%. If the compression had been higher, this could have resulted in a plastic deformation or failure of the

scaffold.

Table 3.4: Results of the compression test. E and k values are represented as mean(SD).

Unit cell	P [%]	Height [mm]	Length [mm]	Area [mm^2]	E [MPa]	k [N/mm]
BC	$50_{\parallel}$	5.5	13.8	190.4	145.5 (20.4)	4855.8 (693.5)
	$50_{\perp}$	5.5	13.8	190.4	185.7 (43.4)	5848.7 (1317.2)
	$70_{\perp}$	8.0	18.8	353.4	135.6 (2.0)	6011.2 (92.2)
FX	$50_{\parallel}$	6.4	14.8	219.0	205.5 (4.3)	7551.7 (126.9)
	$50_{\perp}$	6.4	14.8	219.0	313.5 (13.8)	10710.3 (472.7)
	$70_{\perp}$	9.2	21.8	475.2	144.6 (2.2)	7538.5 (139.0)
T	$50_{\parallel}$	5.7	13.0	169.0	131.8 (1.1)	4203.0 (51.9)
	$50_{\perp}$	5.7	13.0	169.0	185.9 (10.5)	5559.0 (323.5)
	$70_{\perp}$	7.2	16.8	282.2	101.7 (3.9)	4006.9 (139.9)
NP	$50_{\parallel}$	10.1	16.3	265.7	54.9 (1.9)	1468.2 (45.4)
	$50_{\perp}$	10.1	16.3	265.7	144.9 (2.4)	3747.9 (66.4)
	$70_{\perp}$	12.3	19.7	386.1	85.2 (4.0)	2693.5 (119.8)

The stress-strain curves show the differences for unit cell type and 3D-printing direction (Figure 3.7a) whereas in Figure 3.7b the curves show the difference with change of porosity with keeping the unit cell type and 3D-printing direction constant. The flatter the curve, the lower the Elastic modulus for the observed sample.

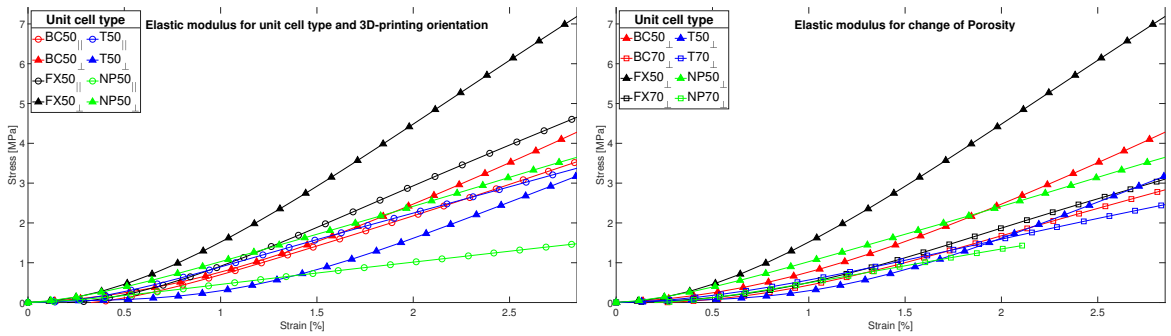

(a) (b)

Figure 3.7: Stress-Strain curves for: a) all unit cell types with 50% porosity and both printing directions, b) all unit cell types with 50% and 70% porosity and perpendicular 3D-printing direction.

To be able to compare the compression test results, since only the 50% parallel and 50% perpendicular scaffolds of same unit cell type had the same area size, the elastic modulus was compared, for either the unit cell type (Figure 3.8a), 3D-printing direction (Figure 3.8b) or the change of porosity (Figure 3.8c).
The FX-cube had the highest mean elastic modulus of all unit cell types with $FX50_{\perp}$ being the highest at 313.5(13.8) MPa. The FX-cube was also the highest in the $50_{\parallel}$ (205.5(4.3)MPa) and the $70_{\perp}$ (144.6(2.2)MPa) group compared to other unit cell types.
BC-cube and T-cube followed with both having similar E values (all not significant) for $50_{\parallel}$ (145.5(20.4)MPa for the BC-cube and 131.8(1.1) for the T-cube (p=0.4296)), $50_{\perp}$ (185.7(43.4)MPa for the BC-cube and 185.9(10.5) for the T-cube (p>0.9999)) and $70_{\perp}$ (135.6(2.0)MPa for the BC-cube and 101.7(3.9) for the T-cube) groups. The other not significant changes were between the $BC50_{\perp}$ and $NP50_{\perp}$ (p=0.2210) and between the $T50_{\perp}$ and $NP50_{\perp}$ (p=0.2180).
The NP-cube had the lowest Young's modulus when compared to other unit cells types, for the same printing direction and/or porosity with the lowest value at 85.2(4.0)MPa for the $NP70_{\perp}$.
The change of 3D-printing direction within the same unit cell type and constant porosity (P=50%) clearly shows, that the perpendicular direction scaffold exhibited a higher strength (Figure 3.8b). The difference between the mean values is 28% for the BC-cube (p=0.2472), 53% for the FX-cube (p=0.0029), 41% for the T-cube (p=0.0116) and 164% for the NP cube (p=<0.0001).
Raising the porosity from 50% to 70%, withing the same unit cell type and constant 3D-printing direction($\perp$)

(Figure 3.8c) results in a noticeable decrease of elastic modulus. Increasing the porosity from 50% to 70% resulted in a decrease of the mean calculated E by 27% for the BC-cube (p=0.1833), 54% for the FX-cube (p=0.0018), 45% for the T-cube (p=0.0022) and 41% for the NP-cube (p=0.0001).

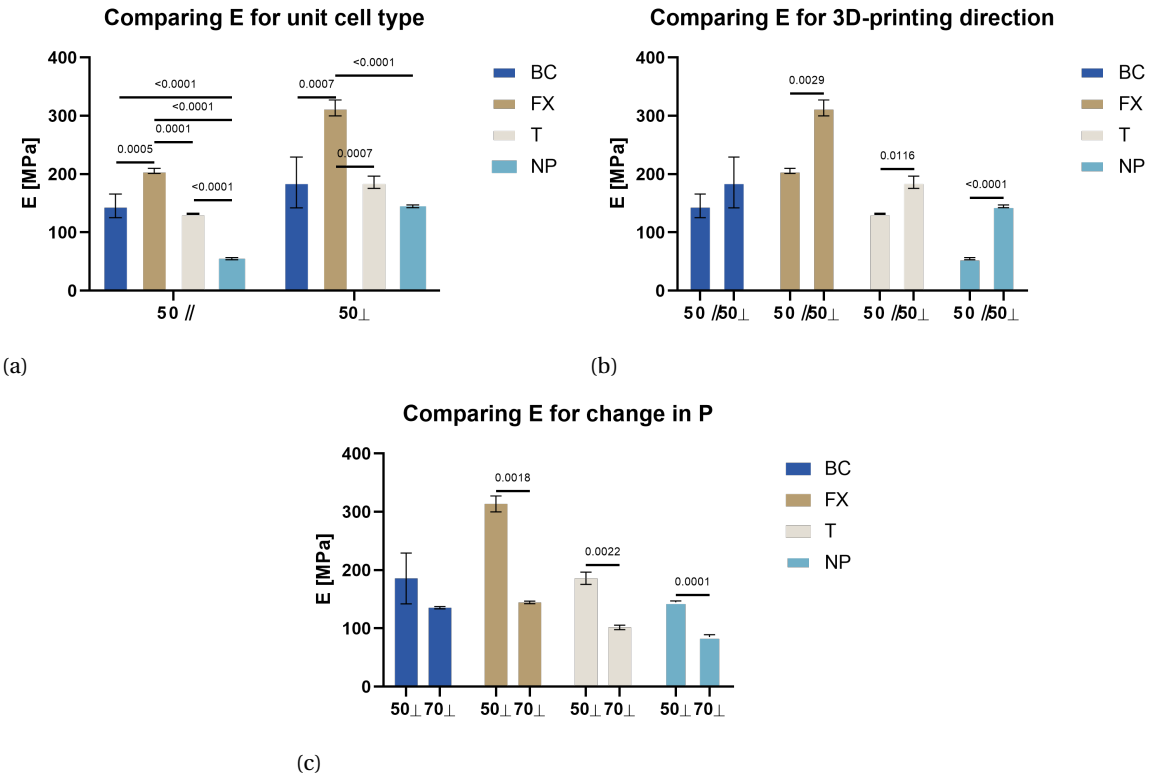

Figure 3.8: Elastic modulus compared for: a) different unit cell types, b) ∥ and ⊥ 3D-printing direction, c) change of porosity.

3.3. Dynamic response

The dynamic test was performed for all unit cell types, 50 and 70% porosity and both 3D-printing directions. The applied oscillation can be seen in Figure 3.9 for the sample which did not break. The acceleration of the input vibration on the bottom cup and the acceleration response of the top cup are plotted. The increase frequency sweep (blue) and the decrease frequency sweep (red) are separated. The peak of the measured acceleration occurs slightly after the direction change of the input frequency sweep. This was a characteristic exhibited by the Instron at higher frequencies.

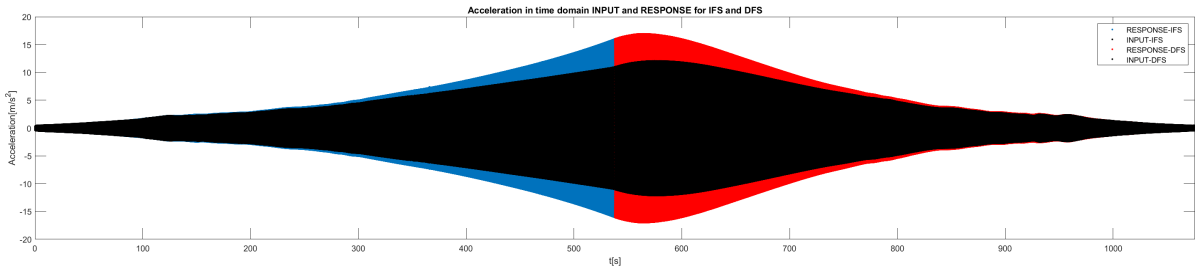

Figure 3.9: An example of the input oscillation and the response in time domain. The input signal on the bottom cup ranged from 10Hz to 60Hz (blue) and back down to 10Hz (red).

If the data is presented in the frequency domain, there are two distinguishable plots. In Figure 3.10a presents the input and response acceleration for the sample which broke during testing. If a failure happened, it occurred in the IFS, therefore the DFS curves of the input and response are not present. However, if a sample did not break (Figure 3.10b), the input and response acceleration are presented for the IFS and the DFS.

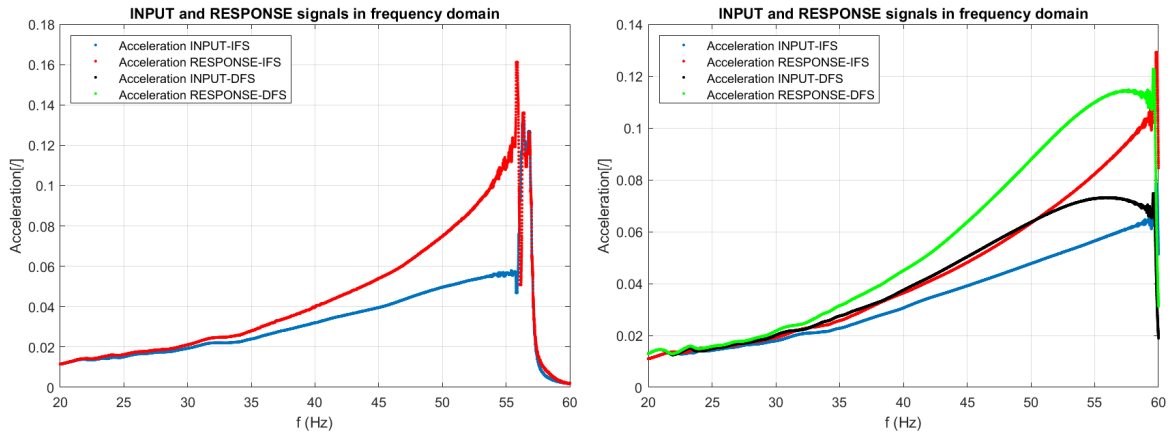

(a) (b)

Figure 3.10: a) Acceleration of the input and response signal for a sample that broke during the test. b) Acceleration of the input and response signal for a sample that did not break during the test. Acceleration values are not accurate to real values, because of the Fourier transform.

To determine the dynamic response of the disc, the ratio between the response and the input signal, called transmissibility function, was determined for the tested frequencies. This function was plotted in the frequency domain for all groups tested (Figure 3.11), with the most common response of the group shown. While most groups showed either failure or no failure for all samples within the group, in two of the twelve groups a combination of failed and non-failed samples were present. In addition, in three groups, there are less samples than planned due to sample failure during the embedding or assembling processes of the dynamic setup.

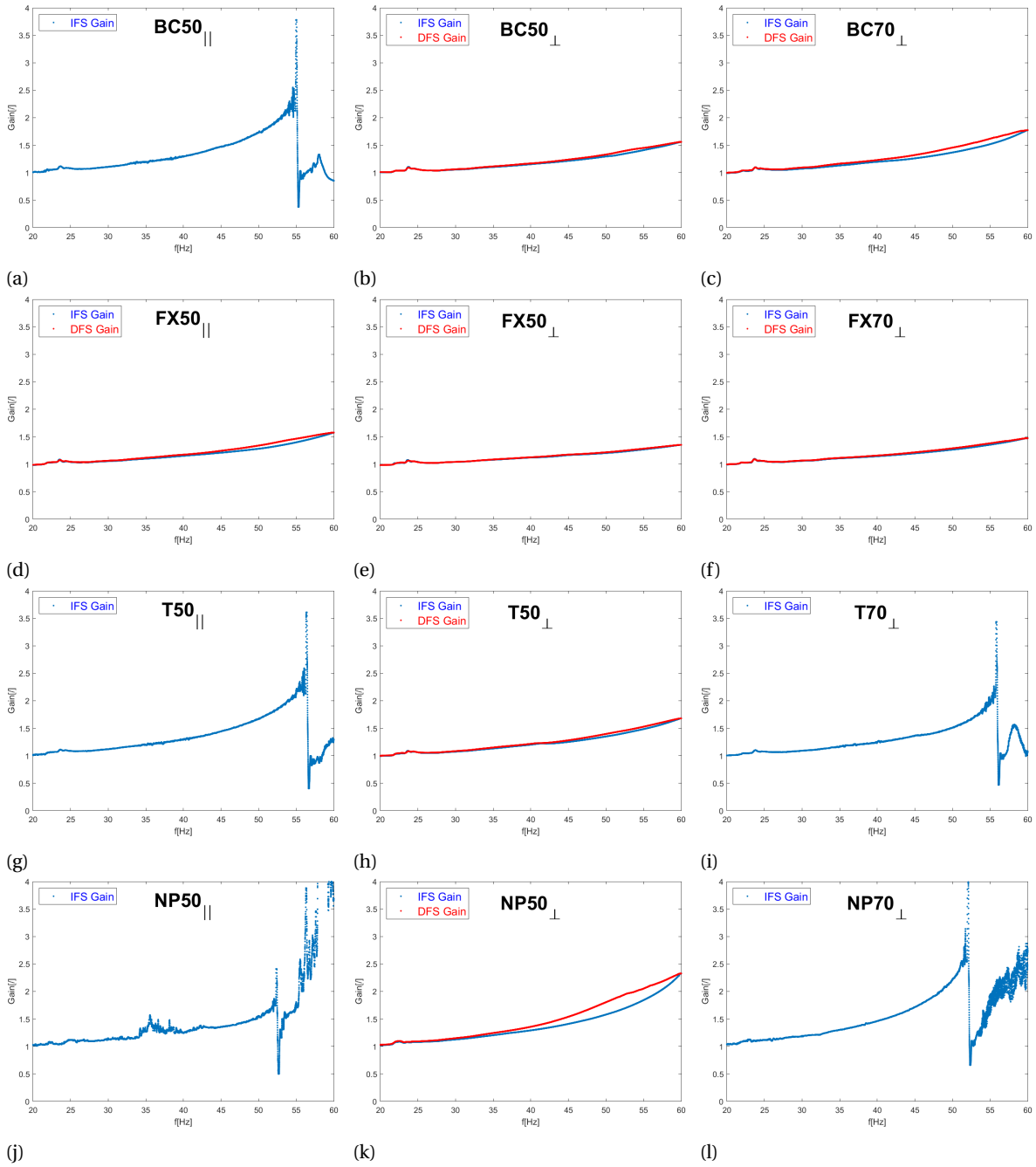

Figure 3.11: Gain plots, showing the most common response of the dynamic WBV testing. The data in the plot is from one sample within the group. The first column represents the $50_{\parallel}$ scaffolds, the second column the $50_{\perp}$ scaffolds and the third column the $70_{\perp}$, while the rows represent the unit cell type, in the following order: BC, FX, T and NP.

The transmissibility peak and break frequency are shown for the tested groups in Table 3.5. Mean values with standard deviation are given if applicable.

Table 3.5: Results of the dynamic test. B-Broken, NB-not broken. Mean and standard deviations () are given. If the sample size is two, the minimum and maximum values are reported.

Unit cell	BC-cube			FX-cube			T-octa			NP-cube		
Porosity[%]	$50_{\parallel}$	$50_{\perp}$	$70_{\perp}$	$50_{\parallel}$	$50_{\perp}$	$70_{\perp}$	$50_{\parallel}$	$50_{\perp}$	$70_{\perp}$	$50_{\parallel}$	$50_{\perp}$	$70_{\perp}$
Nr. of samples: broken | not broken	2B | 1NB	0B | 3NB	1B | 2NB	0B | 2NB	0B | 3NB	0B | 3NB	3B | 0NB	0B | 3NB	3B | 0NB	1B | 0NB	0B | 3NB	2B | 0NB
Peak of transmissibility T [/]	B: 3.78-3.83 NB: 1.79	1.47 (0.08)	B: 3.18 NB: 1.70-1.77	1.57-1.58	1.35 (0.02)	1.57 (0.09)	3.63 (0.07)	1.75 (0.15)	3.59 (0.23)	2.41	2.34 (0.07)	4.08-4.90
Break frequency f [Hz]	B: 54.96-55.86 NB: 60	60	B: 60 NB: 60	60	60	60	56.26 (0.47)	60	55.40 (1.88)	52.32	60	51.98-54.87

If the samples broke, the peak transmissibility magnitude and the frequency are given. If the samples did not break, the peak transmissibility magnitude is displayed, which was always at the highest test frequency of 60Hz. If both cases occurred within a testing group, both results are given.
There were some signal artifacts at low frequencies, while the samples still had no big response. Therefore, the plots are not provided with the actual starting point of 10Hz but only from 20Hz onward.

The FX-cube unit cell had no broken samples during the dynamic testing, no matter of the porosity nor 3D-printing direction. Whereas other unit cell types had no failed samples for perpendicular 3D-printing direction at 50% porosity. The parallel 3D-printing direction at 50% porosity had mostly broken samples except for the FX-cube and one sample of the BC-cube unit cell type. At 70% porosity and perpendicular 3D-printing direction, it was again only the FX-cube and two samples of the BC-cube unit cell type which exhibited no failure during the dynamic testing.

For broken samples, the peak transmissibility magnitude ranged from 2.41 to 4.90, while for the samples which did not break, the measured $T(\omega)$ ranged from 1.35 to 2.34, at the highest frequency input of 60Hz. The frequency at which the samples failed varied from 51.98Hz to 60.00Hz.
Regarding the testing sweep direction of the cases where no failure happened, there is a difference of how the gain returned to 1 at low frequencies between the IFS and DFS. The gain of the DFS stays higher for a longer decrease of frequency until it meets the IFS curve, a kind of hysteresis area. This is more evident for some groups than others.

4

Discussion

IVD degeneration can have severe consequences and is a financial burden, therefore advanced spinal implants, which would replace the IVD and would be resilient to the conditions an IVD faces are needed. There are medical [6] and economical [5] reasons why searching for new designs and concepts in spine surgery technology are important. With 3D-printing as an emerging building technology being broadly applied in the medical field, the lattice structured scaffolds were chosen to be investigated as possible spinal cages. The high porosity of these scaffolds makes it desirable, since nutrient flow and bone growth like such environments. 3D-printing is now allowing us to manufacture such structures, which was not possible before additive manufacturing.
In order to to assess the lattice based IVD implants, four different unit cells were designed and manufactured. A 5x5x2 patterned scaffolds of 50% and 70% with different 3D-printing directions were manufactured. Some designs of the scaffolds had the porosity slightly off the targeted 50% and 70% because of the design process, but the differences were negligible, therefore all scaffolds are described with the same values. Truss thickness was chosen to be constant at 0.8mm to somewhat limit the variables. The scaffolds were designed with porosity in mind but not pore size because it is easier to measure porosity and because porosity seems to be more important for tissue ingrowth as long as the pore size is within a desired range [62].

4.1. Sample characterisation

The overall design of the scaffolds was in the range of the natural IVD for the height, since it is important that the scaffold provides primary stabilization and protects from nerve impingement. The scaffold area is generally smaller than that of human IVDs. This is often the case in spinal fusion implants, because they are stiffer than human IVDs. The other reason is that they could lead to an ideal situation when the implant is fully surrounded by bone to fuse the top and bottom vertebrae and creates a spinal column. In spinal fusion, the use of rods and screws attaching together the neighbouring vertebrae is very common and, therefore, the implant is not the only load bearing device implanted. For this reason the load transmits through several points and could be beneficial in reducing stress shielding.
Build quality was compared with the design and compression mechanical properties were determined. Finally, the response of these scaffolds was observed under dynamic whole body vibrations, to determine how 3D-printed scaffolds react and how different unit cell parameters affect the response. In the future these findings may help design and manufacture scaffolds, that would entail the influence of the dynamic VBW.

The base-scaffold-base design was employed to mimic a FSU, in which the IVD was changed for a spinal cage. The cage is assumed to be well connected with the top and bottom bony vertebrae end plates, with bone ingrowth, which is the goal of the spinal fusion. This presumption allowed us to 3D-print the base-scaffold-base design as one sample and to test it in a way that the scaffold experienced compression and tension during the dynamic testing. If we were to print the scaffolds on their own and test them between two testing plates, when tension occurs, there would be no bond which would pull the scaffolds apart. Nonetheless, it was difficult to determine the properties and build quality of the scaffolds with the two bases being attached. What is more, this design made it more difficult to handle with the samples, especially with the

added embedding and the brittleness of the scaffolds.
The polyet 3D-printing technique used provided us with fairly accurate results. When the density of the 3D-printed parts was compared to the specified density of the raw material, there was a slight decrease of only around 3%, which is to be expected in 3D-printing. This was the result of small imperfections and air pockets in the printed material. When the designed weight of the scaffold was calculated, the new determined density was used.
The build layers were visible under the microscope and in some parts beam fabrication defects were observed while the beam diameter was smaller than the designed dimension. This was especially noticeable in the parallel printing direction which further may have caused a lower elastic modulus compared to the perpendicular direction when compression tests were carried out. For the dynamic testing, the parallel samples were at a disadvantage from the beginning, since it is well known, that tension causes the layer adhesion failure, while tension applied perpendicularly to the printing direction destroys the samples at higher loads. Therefore, a higher failure rate was expected when applying the dynamic test.
Looking at the results for nominal dimensions, the scaffold lengths were close to the CAD design values, whereas the scaffold height had a higher deviation from the design values. However, the variance for both height and length cannot have influenced the later observed mechanical properties noticeably. The deviation between samples in one group does show the nature of the 3D-printing, where imperfections between print parts are observed. However, the 3D-printing direction did influence the nominal size of manufactured scaffolds since an inclination for scaffold length was to be slightly longer for the parallel printing direction. For scaffold height, an inclination was observed that samples printed in the perpendicular direction had higher scaffolds. Comparing the 3D-printed scaffolds to the work of Egan et al.[48], who manufactured similar scaffolds, similar deviations were observed with the scaffolds height being the exception, where slightly larger deviation was measured. As he also observed, there seems to be accuracy dependency on the overall size of the scaffolds, since the scaffolds with 70% porosity, which have larger overall dimensions, are closer to the design dimensions.
From the sample weight measurements compared to the design values, it is not possible to conclude the change of weight of the scaffolds alone, since the scaffolds represent only a minute percent of the total weight. We may assume that the samples as a whole were generally heavier than those designed. This may be due to the fact that the top and bottom bases have larger dimension after printing.

Beam diameter

The beam diameter was set at 0.8mm for all scaffolds, to reduce the variables in the design. The measurements were taken for all scaffolds so that we were able to examine if the unit cell type, 3D-printing direction, the beam orientation and/or the porosity have an influence on the beam diameter dimension. The local beam diameter varied from approximately 0.15mm, being either too large or too small. The mean measurements however had a smaller deviation from the designed value. The range in the local beams was the highest at 0.215mm within a sample group. This shows that within the sample the beam diameter varied noticeably. This could be because of 3D-printing inaccuracy, the differences between the prints at different times, local beam failures and/or imperfect cleaning process.
No apparent connection was seen between the unit cell type and the beam diameter. Similar observations were made for most of the beam orientations, with the exceptions being the 0deg direction having a bias towards the designed value on the S1 side, while the 0/90deg direction beams on the S2 were all higher than the designed values and also higher than the 45deg beams.
When the scaffolds were printed in the parallel direction, all four sides of the scaffolds were equal. Whereas when they were 3D-printed in the perpendicular direction, the side parallel to the printing bed exhibited higher than designed beam diameter dimensions and in general seemed to be less prone to defects. Compression mechanical tests showed that when the layers were parallel to the testing direction, the mechanical properties were stronger and less prone to failure.
When observing the data for the change in porosity (50% compared to 70%) on the S1 side (Figure 3.5a), it seems that at a higher porosity, which also means a higher nominal size, the beam diameter is closer to the design value. On the S2 side (Figure 3.5b), higher porosity(P=70%) produced higher beam diameter dimensions, since in general all values are higher than at lower porosity (P=50%). This could be considered as the same effect as it was observed in the nominal dimensions, i.e. that the beam diameter is accuracy dependant on the scaffold size.

Micro CT

Micro CT scans were taken of the samples to compare the manufactured volume with the design volume. The deviation within the samples was low, which may be interpreted as that the volume did not change immensely within one sample group. All samples had a lower than designed volume, with the closest volume being around 12% smaller than it's equivalent design volume.
The difference between "just scaffolds", which were printed without the base, was compared to the scaffolds printed with the base. The "just scaffolds" were 17.2% smaller than the designed volume while the scaffolds with the base were 22.5% smaller, indicating a difference. This could be because of the base or because of the process of producing the volume models without the bases from the CT scans, whereby some volume could have been lost when cutting away the top and bottom base.
The perpendicular 3D-printing direction had smaller negative deviations from the design volume for all unit cell types, while a higher 70% porosity, compared to a lower 50% one, had a slightly higher volume loss. We observed a lower variance within unit cell types with 70% porosity which were approx. 20% smaller than the CAD design. Whereas a higher variance within unit cell types with 50% porosity was measured, but still at a lower volume than the CAD design for all 50% porosity scaffolds.
For all manufactured scaffolds, a loss of volume is evident, which is an important consideration when designing implants, since a loss of volume might lead to changes in mechanical properties.

4.2. Compression test

Compression tests were performed on all of the samples with the applied strain that did not reach the plastic region and permanently deform and/or damage the scaffolds. This was necessary so the samples could be further used for the dynamic test. According to the initial testing and findings by Egan at al. [48–50, 62, 65], it was determined that up to 3% strain would be safe for all scaffolds, except for the NP-cube at 70% porosity, where 2% strain was applied, as applying more displacement would damage the samples.
The slopes in the linear region of the stress-strain curves (Figure 3.7) show the different elastic moduli that the scaffolds exhibited during the compression test. This value allows us to compare the responses of the scaffolds of different unit cell types, the change of 3D-printing direction and the change in porosity to loading till a strain of 3% or 2% in the case of NP-cube.

If we compare the different four unit cell types used for the scaffold design, the FX-cube stands out with the highest elastic modulus, reaching 313.5 MPa (P=50%, perpendicular 3D-printing direction) and the NP-cube with the lowest with 54.9 MPa (P=50%, parallel 3D-printing direction). These results were expected since in previous observations [48] the reported E value was highest for the FX scaffold as well. The Elastic modulus of the BC-cube was slightly higher than that of the T-cube scaffolds. This is in line with the findings by Egan et al. [65] where the T-cube was reported to have a slightly lower relative elastic modulus. The NP-cube showed the lowest strength compared to other unit cell types for both porosity and both 3D-printing directions.
When comparing the FX-cube elastic modulus to the previous research results [48] ($FX50_{\parallel}$ could be compared), the scaffolds in this Master thesis showed a 32% higher value. For the $BC50_{\parallel}$, the elastic modulus of the scaffold was higher by 24% (compared to [48]) and by 16% (compared to [50]), while for the $BC50_{\perp}$, the elastic modulus of the scaffold manufactured for the purpose of the Master thesis was lower by 18% (compared to [50]), but since the SD was high (44MPa) in this test, the difference could be negligible. In the $BC70_{\perp}$ scaffolds, the elastic modulus for this work showed a 43% higher value than the one reported in the previous tests [50]. The T-cube and NP-cube scaffolds have not been previously tested for mechanical properties, therefore, there was no comparison.
We can conclude that the elastic modulus values are not immensely different if we compare the FX and the BC unit cell types to the previous studies, and especially, when considering the standard deviations within sample groups with a different batch and test dates being a contributing factor. Two other trends are in line with the outcomes of the recent studies, i.e. higher porosity results in lower elastic modulus and parallel 3-D printing direction's lower strength than that of the perpendicular.
Finally, here are the main observations. The FX-cube is the strongest, followed by the BC-cube, T-cube and lastly the NP-cube. The 3D-printing direction had a noticeable effect on the elastic modulus, with all unit cell types presenting higher values (from 28% to 164% higher) for the perpendicular direction. A higher porosity within a unit cell type leads to a lower Young's modulus (from 27% to 54% lower).

The stiffness of the scaffolds ranged from 1.5 kN/mm to 10.7 kN/mm. An additive manufactured titanium cage [68] also using a truss-based design, had a stiffness of 31.2 kN/mm whereby the implant area was 300mm^2. This shows that metal 3D-printed implants are much stiffer with the traditionally manufactured metal cages having even higher stiffness values. A increase of the scaffold area leads to higher stiffness, which could be a solution if the stiffness was too low for the 3D-printed polymer scaffold. However, due to stress shielding, the lower stiffness of the scaffolds would be advantageous and could lead to a lower failure rate intended to be applied in spinal fusion. In a study [69], where they compared PLLA cages with reduced stiffness to a stiffer titanium cage, cages with lower stiffness showed significant enhancement in lumbar interbody fusion. The PLLA cages with lower stiffness ranged from 2-4kN/mm, which is in the range of cages designed and manufactured in this study. Such lower stiffness would also not present many mechanical stability problems, as rods and screws are typically used to help fix the neighbouring vertebrae.

4.3. Dynamic response

Dynamic whole body vibration was applied to all unit cell types, 3D-printing directions and porosity using a testing setup from a previous study used on human FSUs. The setup and applied displacement mimicked a base excitation model.
Since the position of the accelerometer which collected the input acceleration (from the Instron actuator) was not measured at the bottom cup, but was moved to the adapter plate, a test was performed to determine the influence of the position (Figure 4.1a). The first accelerometer was put on the bottom plate and the second on the adapter plate. The gain was observed from the collected accelerations in the frequency domain (Figure 4.1b). Since the gain stays at around 1 for the whole testing range, it is fair to say, that the position of the accelerometer did not affect the testing results.
The second control test was conducted to determine that the compliance of the top plate, the restraining cylinder, the crossbar, the weights and the weight holders assembly was adequately low and would not introduce any significant errors into the measured response of the free floating top base of the sample. Therefore, a solid stainless steel cylinder was fitted in the place of the sample and was fastened to the top and bottom plate (Figure 4.1c). The gain was observed between the top and bottom cup (Figure 4.1d). It was estimated to be around 1 for all of the testing range, indicating that the top assembly parts were rigid and the connections among them were adequately tight. The low compliance of the top assembly guarantees that the testing results are not influenced by the top assembly.

If we look at the results of the dynamic test, we can see that the scaffold had a response at high frequencies, compared to what was seen on human IVDs [24]. The scaffolds had a notable response upwards of 50Hz if they were damaged or undamaged. If the samples did not break, the peak transmissibility value could give some clues if the sample was close to breaking, with lower values indicating stronger characteristics against dynamic loading. The scaffolds showed a nonlinear response to dynamic loading, since the increase of the gain was rapidly increasing before a failure.
Concerning the influence of the unit cell type, the FX-cube seems to be most resistant to such dynamic loading, with no sample failures occurring. The FX-cube had also the highest elastic modulus values of the unit cell types, which may lead to the conclussion that a higher elastic modulus is favorable for scaffolds protection against failure. The BC-unit cell type, which exhibited a slightly lower Young's modulus than the FX-cube, also showed good resilience against WBV, since the majority of its scaffolds survived.
However, in testing the T-octa and NP-cube unit cells, most of the test samples broke and are therefore less resilient to dynamic loading.
Within the unit cell types when comparing frequencies at which the samples broke it was discovered that the BC-cube and T-octa have similar values for $50_{\parallel}$, and that they are both higher than for the NP-cube. This was expected since the NP-cube has a lower E value and sample failure at lower frequencies was the result of this. The same was also evident for the $70_{\perp}$ group. Whereas for the $50_{\perp}$, where no failure was present, we can observe the peak transmissibility. The FX-cube had the lowest value at 1.35(0.02), followed by the BC-cube 1.47 (0.08), T-octa 1.75 (0.15) and the NP-cube 2.34 (0.07). This order indicates that regarding dynamic loading the FX-cube is most resilient while the NP-cube is least resilient to dynamic loading.

The influence of the 3D-printing direction on the dynamic response was clear. The perpendicular direction samples exhibited no failure, whereas the parallel direction samples mostly failed. The FX-cube, which in general seemed to be strong enough to withstand the dynamic testing, had no failure but we can still com-

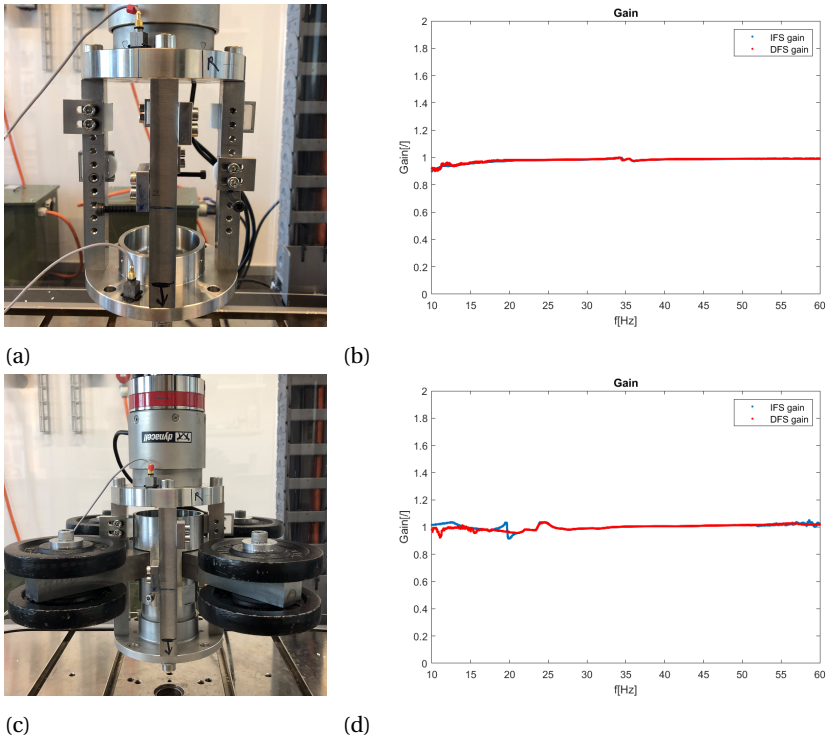

(a) (b)

(c) (d)

Figure 4.1: a) Mechanical setup where the influence of the position of the accelerometer sensor was observed. b) Gain plot of the data collected from both positions and compared. c) Mechanical setup where the top assembly was tested, if it had any large dynamic response to the input signal from Instron. d) Gain plot showing the response of the top assembly to the input signal from Instron.

pare the peak $T(\omega)$ values. The perpendicular direction had a lower value of 1.35 (0.02) compared to the 1.57-1.58 value of the parallel direction, at the same porosity, which may indicate that for the FX cube the perpendicular direction is more resistant to dynamic loading.

The increase of porosity from 50% to 70% has shown similar results as the compression test, where at higher porosity the scaffolds had a lower elastic modulus. The higher porosity decreases the resistance capability of the scaffolds to dynamic loading. This was most evident for the T-octa and NP-cube unit cell types, where all scaffolds broke at the higher porosity compared to no broken scaffolds at the lower porosity. For the FX-cube, a stronger scaffold was observed at 50% porosity at $T(\omega)$=1.35 (0.02) compared to $T(\omega)$=1.57 (0.09). Moreover, at 50% porosity, the BC-cube experienced the highest peak at 1.47 (0.08) compared to 1.70-1.77, indicating a higher load-carrying capacity scaffold at lower porosity.

For the samples where no failure occurred, a difference between the IFS and DFS can be observed. The difference, displayed in the shape of a hysteresis, is the largest in the first 20Hz decrease from 60Hz for all sample groups. Groups with a lower elastic modulus showed larger IFS-DFS differences. For example, the NP50$_\perp$ (Figure 3.11k)had a low Young's modulus and showed a high response which may be interpreted that the sample was close to failure. The FX50$_\perp$(Figure 3.11e) which had a very high elastic modulus when compared to others showed almost no difference between IFS and DFS. If the test was performed up to higher frequencies, a bigger difference between IFS and DFS would be exhibited.

If we compare the results of the dynamic test to the results of the human IVD dynamic test on the same testing setup it may be assumed that the tested scaffolds are more resistant to such dynamic loading. Marini et al. [24] showed a jump phenomenon, where the scaffolds are at risk of failure, occurring at frequencies ranging from 34.25 to 40.92Hz, at the same preload (16kg) and displacement (0.1mm) which was also the case in this master thesis. For the samples used in this thesis, the lowest frequency at which the scaffolds failed was at 51.98Hz. This shows that the scaffolds designed and manufactured in the above described way, are capable of withstanding higher dynamic loads than human IVDs.
It is interesting to note that studies, albeit employing the discrete frequency testing method unlike the one

used in this thesis, have shown the range of resonance of the IVD to be from 8.0-10.4 [27] and 23.5-33 [33]. This range is again well below the results we obtained from the 3D-printed scaffolds. Therefore, considering the response of the scaffolds to such base excitation like dynamic loading, we may assume, that lattice-based structures like these should withstand these loads.

4.4. Future perspectives

The design of the lattice-based IVD implant could be further investigated further, with either other or existing unit cells, with changing the truss diameter and adding reinforcements or other features and observing the mechanical properties and the response to WBV. While we examined the change of homogeneous porosity of the scaffolds, it would be interesting to investigate a change of porosity withing a scaffold, possibly making it less porous around the exterior walls and gradually increasing the porosity towards the centre of the spinal implant. This would make the scaffold stiffer on the outside and less stiff towards the center.
For the purpose of this Master thesis, we have chosen to control the porosity and not the pore size of the scaffolds. Since pore size may be important when implants are concerned, the influence of pore size on other properties of the scaffold could be investigated.
Today, 3D-printing may be applied to various kinds of materials, not just polymers but also metals, ceramics and others. Therefore, it may be beneficial to investigate other applicable materials, which could better promote osteointegration or have better specific material properties. Further, it would be sensible to explore what kind of mechanical properties such materials provide in lattice-based implants and how they respond under WBV dynamic testing.
While the polyet 3D-printing technique provided us with fairly good accuracy, it was still evident that 3D-printed parts had some errors and the layers were distinguishable. Therefore, the material was not homogeneous. Consequently, new 3D-printing techniques should be explored, which will produce a more homogeneous material within the sample and would improve the build accuracy of new implants.
The compression test to determine the Young's modulus and compressive stiffness is the most commonly used mechanical test to determine spine implant properties. However, there are other quasi-static tests, such as tension, flexion, shear and torsion tests, which could lead to a deeper insight in examining the question whether the IVD implant is able to withstand all the loads occurring in the spine.
In future research, a different testing setup of IVD implants under WBV should be developed. This should allow for an easier and faster mounting of the implants, especially there should be no need to have an embedding system, but it should still mimic a base excitation model. In addition, using implants without the attached bases as was not the case in this study, is closer to a real life implantation situation as the base could influence the mechanical behaviour of the implant. Hence, one should design a system which transfers tension loads during the dynamic testing similar to what an implant would experience in the spine while it keeps the mounting of the implants simpler. The mechanical testing setup applied in the current study was also extremely difficult to handle because it was not only heavy but also demanding a high level of caution, not to break the samples during the mounting procedure. In future experiments, the effect of the preload and the applied amplitude on spinal implants, as was done by Marini et al. ([24]) on human IVDs, should be investigated to determine if it has a similar effect on the implants under dynamic testing.

5

Conclusion

A base-scaffold-base structure was designed mimicking the FSU, which successfully enabled mechanical testing of the scaffolds for different unit cell types, parallel and perpendicular 3D-printing directions and 50/70% porosity. In terms of the design and build quality it may be assumed that the polyet 3D-printing technology was adequate, for it managed to produce the fine structures of the scaffolds fairly well. However, because of the nature of the additive manufacturing process the the printing direction was seen as an important factor of the scaffold properties. The printing direction to testing direction dictated how much the scaffolds could withstand during testing. Also the detected beam fabrication defects observed throughout the scaffolds tended to weaken the whole structure and provided weak points inside, where the scaffold could fail first and resulted in a rippling effect. Therefore, better layer adhesion, which would lead to more homogeneous parts, would be beneficial in producing implants that must withstand mechanical loading.
Depending on how strong the implant needs to be for the intended use, the four unit cell types offer a range of options due to their different load-carrying capacities. Further, one may play with different levels of porosity to achieve a good balance between the mechanical properties and bone promoting characteristics. Previous knowledge of the unit cells showed that the BC-cube had already appeared favourable across different parameters, such as surface to volume ratio and permeability. In this thesis, the BC unit cell seemed fairly equal with the FX and T unit cells for the characteristics tested. The FX-cube had a higher stiffness, but this may not always be desirable due to stress shielding. A stiffness of around 2-4kN/mm was shown to be advantageous for lumbar interbody fusion [69].
The influence of porosity and 3D-printing directions provides an option. For example, if any chosen unit cell is desirable because of other properties (tension properties, shear modulus, surface-volume ratio, permeability), it is fairly simple to change the design or printing parameters and obtain the desired results. This would further allow for the user to design and manufacture specific implants accommodated for location and function and not only for application of the spinal cage implants. In order to produce safe implants, improved 3D-printing quality or a scaffold design where such additive technique could be safely used will have to be considered. The 3D-printing direction seems to be a considerable factor if the samples have to withstand a high load, whereas the porosity is on the one hand desired to be higher for a better bone growth but on the other should not rise too high because then the scaffold would not be strong enough.

The dynamic response to base excitation dynamic loading showed that the scaffolds with the current designs and 3D-printing technique can withstand higher frequencies than human IVDs at the same preload and displacement. This shows a good promise for future truss-based scaffolds since they have higher failure frequencies than the reported resonant frequencies that can be detrimental for even healthy discs.
The design of the unit cell type does have a clear influence on the response to WBV. The FX-cube showed the best response with no failed sample regardless of printing direction or porosity, while the NP-cube's reaction was the weakest. However, all of the samples showed to be capable of surviving at least to 50Hz.
The influence of the 3D-printing direction was also evidently more substantial in the perpendicular direction, with all $50_{\perp}$ direction scaffolds surviving and most $50_{\parallel}$ direction failing. As already observed in compression tests, the influence of the direction of the 3D printed layers compared to the test direction seems to be very influential on the mechanical properties, which is often observed in 3D printed parts. During the dynamic test carried out in this thesis, the scaffolds experienced compression and tension. The parallel 3D- printed

scaffolds were much less able to withstand the tension forces that pulled the layers apart. Therefore, based on the general knowledge of 3D printing, it was expected that the parallel samples would fail first. There were also many printing errors in the parallel direction, which most likely had a negative effect on the dynamic response.
The higher the porosity, the lower the mechanical properties, with the same material and design. This has been shown for the elastic modulus and also applies to the dynamic behavior. Scaffolds with a higher porosity tended to fail at lower frequencies than scaffolds with the same unit cell type and 3D printing direction at a lower porosity. Therefore, it can be said that lower porosity leads to failure at higher frequencies. The response of the lattice-based scaffolds when using a base excitation model for a broad frequency range that simulates WBV conditions is nonlinear because the response of the scaffolds increases rapidly before failure. This has also been observed in human IVDs.
As soon as the scaffolds failed, the connection between the upper and lower part of the scaffold was gone and therefore the tensile tension forces could not be transmitted. In contrast, after a jump phenomenon in human IVDs [24] the connection was still there and the reaction could be further observed.
In terms of dynamic response, the results of this work suggest that the FX-cube design is the most resistant and would improve the safety of the implant. For the 3D printing direction, we concluded that the perpendicular direction, i.e. the layers are perpendicular to the testing direction, is the one that can best withstand the dynamic forces. Porosity should also be an important design parameter, as a change in porosity showed a different response for all designs. Therefore, the unit cell design, 3D printing direction, and porosity should be important in the design of the lattice-based spinal implants that are to withstand WBV, with many other parameters, such as pore size, truss cross section geometry and material choice likely to have a significant impact as well.

There have been some limitations in the research into lattice-based spinal cage scaffolds. If the 3D printing quality had been better, the design features would have been more precisely printed and there would be less printing errors in general. This would most probably lead to a lover variation within the sample groups.
To compare stiffness values for different unit cell types, the nominal area of the samples would need to be the same. This would reduce the variable of scaffold size and give us an additional comparison.
For the NP-cube only one negative Poisson's value was tested and the influence of the change of the value was not investigated. In addition the Poisson's number was only calculated with the design dimensions, but was not experimentally determined, because it is not trivial to practically determine this value. The NP unit cell type was also the only one using square beam cross-section, compared to the octagonal for the other three unit cell types. This difference in beam cross-section geometry could have led to some differences in properties of the scaffolds, but was not investigated.
There are many more mechanical properties that were not determined and could be of importance when designing implants. For spinal cage implants, the tension, shear and torsion tests could have been beneficial to run, since the implants would most likely experience these loads when implanted.

6

Abbreviations

- ADR - Artificial disc replacement
- AF - Annulus fibrosis
- BC cube - Body centered cube
- CAD - Computer-aided design
- CEP - Cartilaginous end plates
- CT - Computed tomography
- DAQ - Data acquisition
- DDD - Degenerative Disc Disease
- DH - Disc herniation
- EZ - Elastic zone
- FSU - Functional spinal unit
- FX cube - Face centered cube
- IDD - Internal disc disruption
- IVD - Intervertebral disc
- LBP - Lower back pain
- NP - Nucleus pulposus
- NP cube - Negative Poisson's ratio cube
- NZ - Neutral zone
- PP - Posterior surgical procedure
- T octa - Truncated octahedron
- TDR - Total disc replacement
- WBV - Whole body vibration

A Appendix

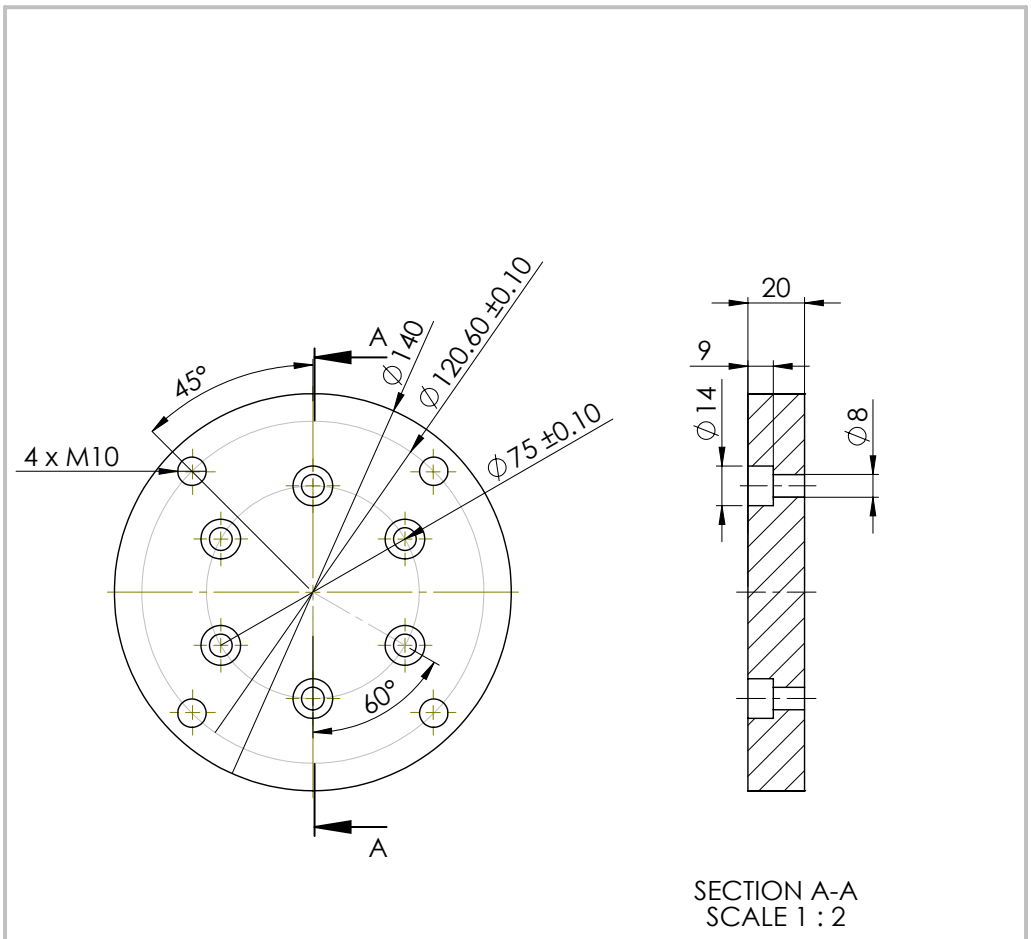

Chamfer edges and holes 45 x 0.5

ETH zürich Laboratory for Orthopaedic Technology				Allgemeintoleranzen ISO 2768 - fK Oberflaechenbeschaffenheit ISO 1302 **MASSSTAB: 1:2**	BENENNUNG: Top Adapter for Instrom E10000 Ø140x20
	NAME	SIGNATUR	DATUM	WERKSTOFF:	ZEICHNUNGSNR.
GEZEICHNET	Jaka Pizorn		22. 2. 2019	Stainless Steel	TopAdapter_InstromE10000
GEÄNDERT					
GEPRÜFT				**REV. A**	BLATT 1 VON 1

B Appendix

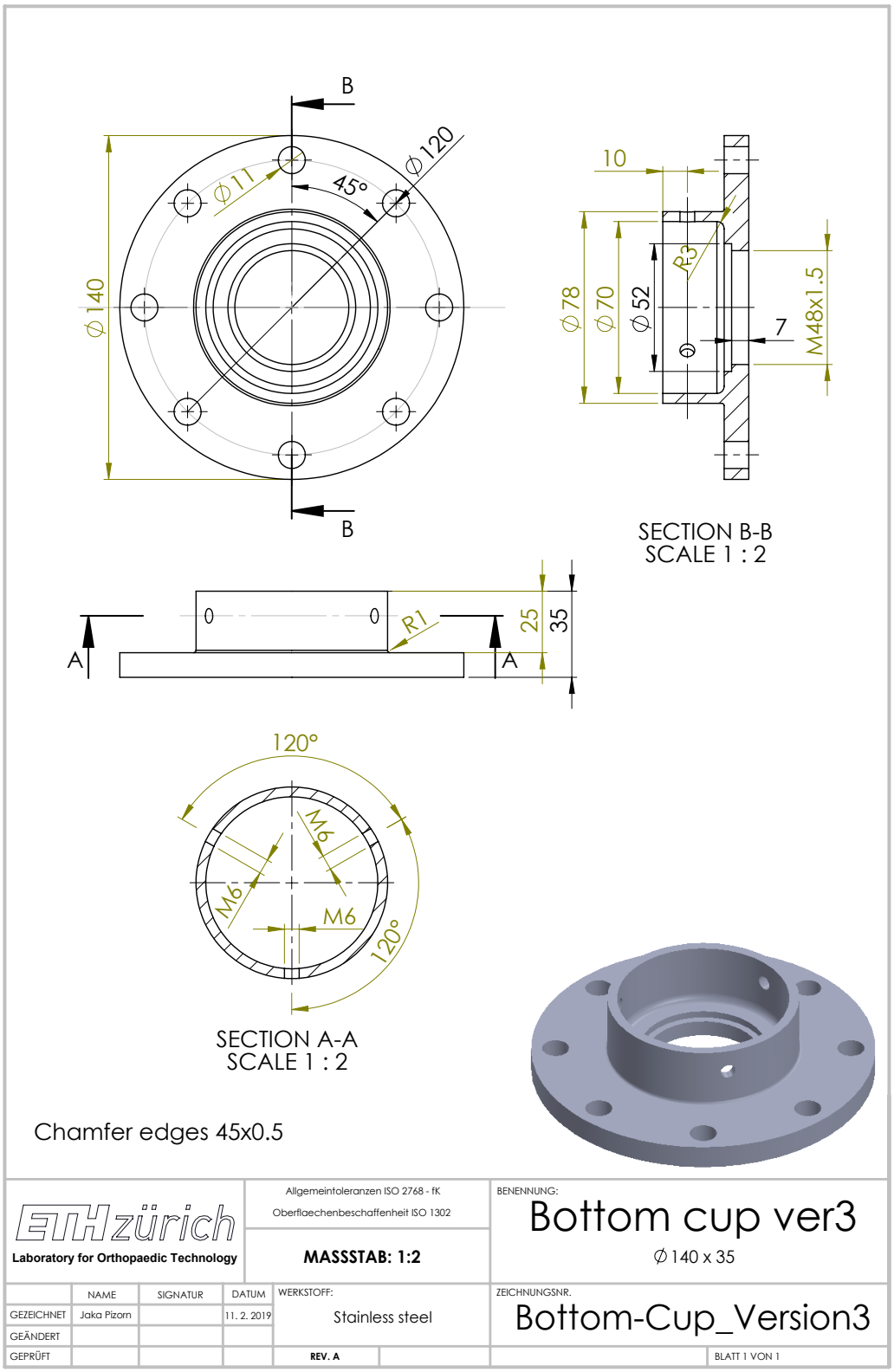
B
⌀120
⌀11
45°
⌀140
B
10
⌀78
⌀70
⌀52
R3
7
M48x1.5
SECTION B-B
SCALE 1 : 2
A
R1
25
35
A
120°
M6
M6
M6
120°
SECTION A-A
SCALE 1 : 2
Chamfer edges 45x0.5
ETH zürich
Laboratory for Orthopaedic Technology
Allgemeintoleranzen ISO 2768 - fK
Oberflaechenbeschaffenheit ISO 1302
MASSSTAB: 1:2
BENENNUNG:
Bottom cup ver3
⌀140 x 35
NAME
SIGNATUR
DATUM
GEZEICHNET
Jaka Pizorn
11. 2. 2019
GEÄNDERT
GEPRÜFT
WERKSTOFF:
Stainless steel
REV. A
ZEICHNUNGSNR.
Bottom-Cup_Version3
BLATT 1 VON 1

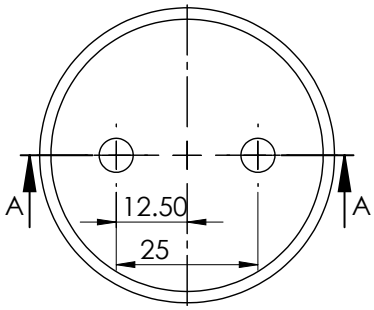

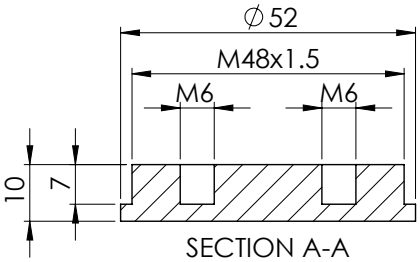

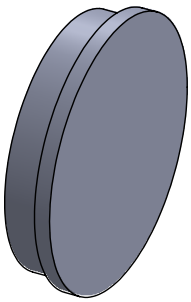

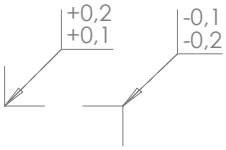

Chamfer edges 45x0.5

ETH zürich Laboratory for Orthopaedic Technology		Allgemeintoleranzen ISO 2768 - fK Oberflaechenbeschaffenheit ISO 1302 **MASSSTAB: 1:1**		BENENNUNG: Bottom Cup Screw M48x10	
	NAME	SIGNATUR	DATUM	WERKSTOFF:	ZEICHNUNGSNR.
GEZEICHNET	Jaka Pizorn		11. 2. 2019		Bottom-Cup-Screw _cylinder-Version3
GEÄNDERT					
GEPRÜFT				**REV. A**	BLATT 1 VON 1

C Appendix

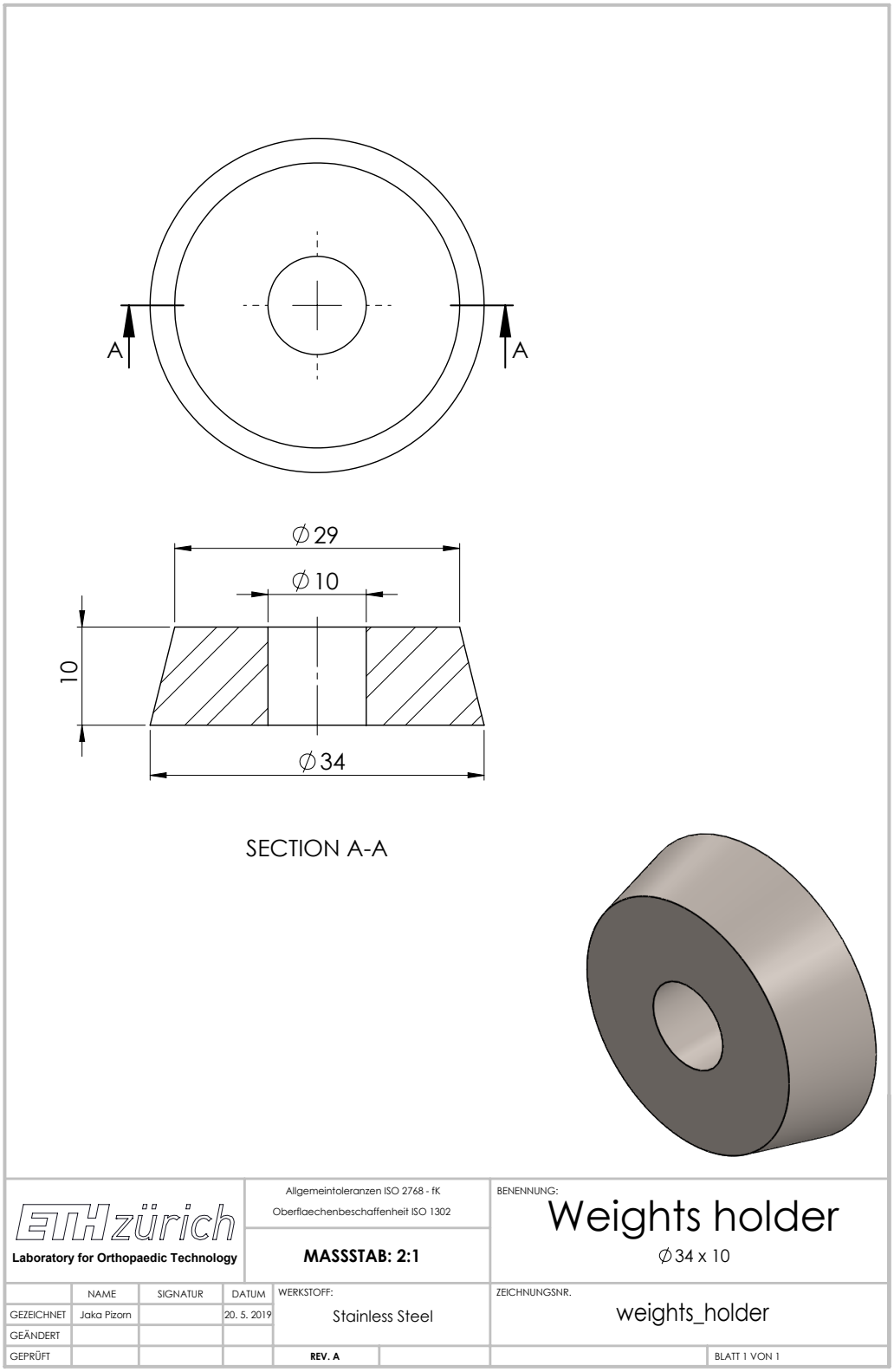
A
A
∅29
∅10
10
∅34
SECTION A-A
ETH zürich
Laboratory for Orthopaedic Technology
Allgemeintoleranzen ISO 2768 - fK
Oberflaechenbeschaffenheit ISO 1302
MASSSTAB: 2:1
BENENNUNG:
Weights holder
∅34 x 10
NAME
SIGNATUR
DATUM
GEZEICHNET
Jaka Pizorn
20. 5. 2019
GEÄNDERT
GEPRÜFT
WERKSTOFF:
Stainless Steel
REV. A
ZEICHNUNGSNR.
weights_holder
BLATT 1 VON 1

D Appendix

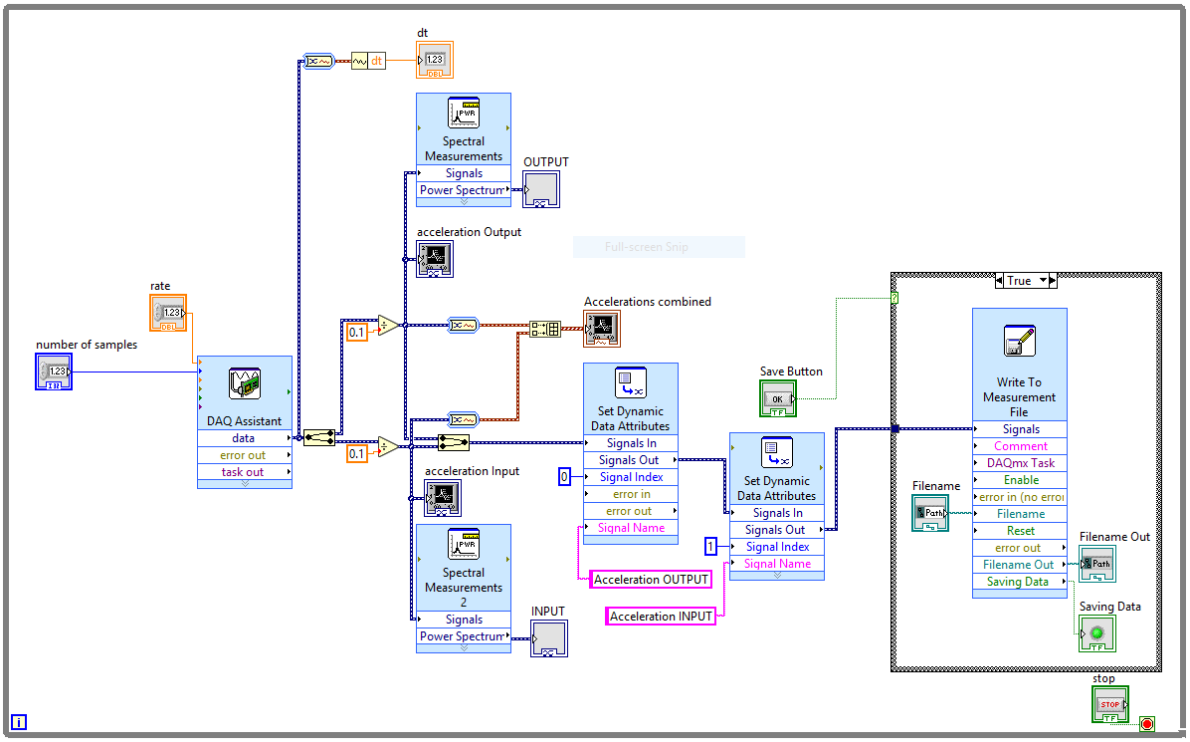
dt
Spectral Measurements
Signals
Power Spectrum
OUTPUT
acceleration Output
Accelerations combined
rate
number of samples
DAQ Assistant
data
error out
task out
0.1
0.1
acceleration Input
Set Dynamic Data Attributes
Signals In
Signals Out
Signal Index
error in
error out
Signal Name
Save Button
Set Dynamic Data Attributes
Signals In
Signals Out
Signal Index
Signal Name
Acceleration OUTPUT
Acceleration INPUT
Spectral Measurements 2
Signals
Power Spectrum
INPUT
True
Write To Measurement File
Signals
Comment
DAQmx Task
Enable
error in (no error)
Filename
Reset
error out
Filename Out
Saving Data
Filename
Filename Out
Saving Data
stop

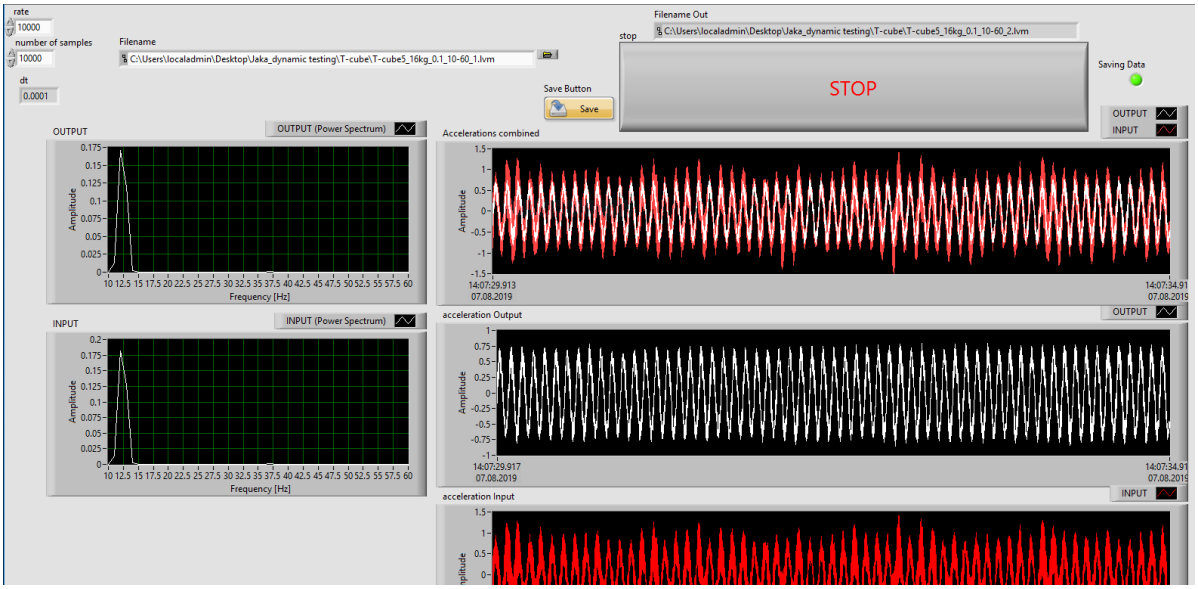
rate
number of samples
dt
Filename
Save Button
Save
stop
STOP
Filename Out
Saving Data
OUTPUT
OUTPUT (Power Spectrum)
Accelerations combined
INPUT
INPUT (Power Spectrum)
acceleration Output
acceleration Input
Amplitude
Frequency [Hz]

E Appendix

```
% Jaka Pizorn, 28.6.2019, Zurich
clc; clear all; format longG

load ("BC_cube.mat"),load ("FX_cube.mat"),load ("T_cube.mat"),load
 ("NP_cube.mat") % Loads the samples, their x,y and h measurments
 taken with a caliper

for ii=1:4

iii=num2str(ii);
filename='BC-cube1_3strain_.steps.tracking.csv'; %Input the name of
 the sample
newStr = insertBefore(filename,'.steps.tracking.csv',iii);
[filepath,name,ext] = fileparts(newStr);
B1 = regexp(name,'\d*','match');             % get data from name of
 the file, frequency start and freq finish
B=str2double(B1);
C1='BC';
C2='FX';
C3='T';
C4='NP';
% Check the filename to find out which unit cell
TF1 = contains(filename,C1);
TF2 = contains(filename,C2);
TF3 = contains(filename,C3);
TF4 = contains(filename,C4);
% When you know the unit cell, load the x,y,h from the
 coresponding .mat files
if TF1==1
    kk = find(BC_cube==B(1));
      x=BC_cube(kk(1),2);
      y=BC_cube(kk(1),3);
      h=BC_cube(kk(1),4);
elseif TF2==1
    kk = find(FX_cube==B(1));
      x=FX_cube(kk(1),2);
      y=FX_cube(kk(1),3);
      h=FX_cube(kk(1),4);
elseif TF3==1
    kk = find(T_cube==B(1));
      x=T_cube(kk(1),2);
      y=T_cube(kk(1),3);
      h=T_cube(kk(1),4);
elseif TF4==1
    kk = find(NP_cube==B(1));
      x=NP_cube(kk(1),2);
      y=NP_cube(kk(1),3);
      h=NP_cube(kk(1),4);
    else
        fprintf('No correnct file was input')
end
```

```
A3=x*y; %[mm] Area of scaffold
E1=1600; %[MPa] =E2, from solid 3D printed material

A=dlmread(newStr,',',1,0); %load data from Instron, perpendicular
 parallel
Load=A(:,9)*1000; %[N]
Displacement=A(:,10); %[mm]

i=1;
while Displacement(i,1)>min(Displacement) %Find the Displacement
 data only for when compressing and not also when releasing,,
 min(Displacement) finds the min displacement value
    D(i,1)=Displacement(i,1);
    i=i+1;
end
D=D(1:round(length(D)*1)); % delete a few points at max displacement,
 because there is some weird data, probably because of Instron
 changing direction
Load1=Load(1:length(D)); %Load data only for when compressing and not
 also when releasing
D_1=D;
L_1=Load1;
r=1;
while Load1(r,1)>-5
    A=r;
    r=r+1;
end
L=Load1(A+1:end);
D=D(A+1:end);

p = polyfit(D,L,5);
L=polyval(p,D);
l=length(D);
D=D-D(1);
L=L-L(1);
```

plot Force-displacement curve

```
%going from X% displacement to X% displacement to determine the
 stiffness and E
b1=0.55;            %percent of max displacement to the begin the
 linear part
b2=0.9;             %percent of max displacement to the begin the
 linear part
l1=length(D)*b1;    % set the begining point from where it is assumed
 that it linear
l1=round(l1);
l2=length(D)*b2;    % end point
l2=round(l2);

linD=[D(l1) D(l2)]';
linL=[L(l1) L(l2)]';
```

```
k = diff(linL)./diff(linD); % Stiffness of the sample [N/mm]= the
 slope of the linear part of the measurement that we have pre-
determined
Ex=k*h/A3; % Elastic modulus from 2 point defined line [MPa]
figure(1)
subplot(2,1,1)
plot(D_1,L_1,'.',D,L,'.k',linD,linL,'r')
xlabel(['Displacement [mm]'])
ylabel(['Force [N]'])
```

Stress-Strain curve

```
stress=L/A3; %[MPa] stress for the scaffold only, equation above
strain=D/h; % [/]

lin_strain=[strain(l1) strain(l2)]';
lin_stress=[stress(l1) stress(l2)]';

figure(1)
subplot(2,1,2)
plot(strain*100,stress,'-.',lin_strain*100,lin_stress,'r')
xlabel(['Strain [%]'])
ylabel(['Stress [MPa]'])

CCC(ii,1)=Ex; % for each sample of a specific unit cell, 4
 compressiont est were done and the E moduli calculated for each and
 added in the first column
CCC(ii,2)=k; % for each sample of a specific unit cell, 4 compressiont
 est were done and the stiffness k calculated for each and added in
 the second column
ii=ii+1;

end

fprintf('For sample %.9s:\n',filename)
fprintf('E[MPa] k[N/mm]\n')
fprintf('%2.2f %2.2f\n',[CCC(:,1),CCC(:,2)].')
```

Published with MATLAB® R2018a

F Appendix

```
% Jaka Pizorn, 2019 Zurich
clc;
clear all;

tt=0;                                   % signal that you want to delet
 in the beggining [s]
beginOffset=10000*tt;
filename='BC-cube9_16kg_0.1_10-60_1.lvm';
[filepath,name,ext] = fileparts(filename);
B = regexp(name,'\d*','match');         % get data from name of the
 file, frequency start and freq finish
B=str2double(B);

A=dlmread(filename,',',23,0);           %load acceleration data
 from .lvm file [beginOffset+23 0 500000 1]
A = array2table(A);
accINPUT1=A{:,3};                       % Input means accleration data
 collected on the bottom cup
accRESPONSE1=A{:,2};                    % Response means acceleration
 data collected on the top cup
T=A{:,1}(2)-A{:,1}(1);                  % Sampling period
Fs=1/T;                                 % Sampling frequency
% Define these things for each test
f_range=[B(5) B(6)];                    % range of x axis in frequncy
 domain [Hz]
sweep_rate=0.1;                         % Frequency sweep rate up and
 down [HZ/s]
sweep_time=(B(6)-B(5))/sweep_rate+38;   %time to sweep from start freq
 to end freq
end_IFS=(sweep_time/T)+1;               %point where the IFS sweep has
 ended, determined by sweep rate and the freq range
end_DFS=2*(sweep_time/T);               %point where the DFS sweep has
 ended, determined by sweep rate and the freq range

d = designfilt('lowpassiir', ...        % Response type
       'PassbandFrequency',75, ...      % Frequency constraints
       'StopbandFrequency',120, ...
       'PassbandRipple',0.1, ...        % Magnitude constraints
       'StopbandAttenuation',200, ...
       'DesignMethod','butter', ...     % Design method
       'MatchExactly','passband', ...   % Design method options
       'SampleRate',Fs);                % Sample rate

%Apply the filter
accINPUT = filter(d,accINPUT1);          %apply filter on acceleration
 INPUT
accRESPONSE= filter(d,accRESPONSE1);     %apply filter on acceleration
 RESPONSE

i=1;
while accINPUT(i)<0.1                    % This finds how much data
 must be removed in the beginning
```

```
    i=i+1;
end
OriginalInput=accINPUT1(i-1:end);       %remove data before the
 beginning of the test
OriginalOutput=accRESPONSE1(i-1:end);   %remove data before the
 beginning of the test
accINPUT=accINPUT(i-1:end);             %remove data before the
 beginning of the test
accRESPONSE=accRESPONSE(i-1:end);       %remove data before the
 beginning of the test
t111=linspace(0,T*length(OriginalInput),length(OriginalInput))';
%Determening values from input data
l=length(accINPUT);                     % Length of signal
NFFT = 2^(nextpow2(Fs)+8);
t=linspace(0,T*l,l)';                   %time vector
f = Fs*(0:(l/2))/l;                     % Fs/2*linspace(0,1,NFFT/2+1);
nfft=2^nextpow2(l);
if length(accINPUT)>end_IFS
accINPUT_IFS=accINPUT(1:end_IFS);           % IFS acceleration data
 INPUT
accRESPONSE_IFS=accRESPONSE(1:end_IFS);     % IFS acceleration data
 OUTPUT
accINPUT_DFS=accINPUT(end_IFS:end);           % IFS acceleration data
 INPUT
accRESPONSE_DFS=accRESPONSE(end_IFS:end);     % IFS acceleration data
 OUTPUT
% accINPUT_DFS=accINPUT(end_IFS:end_IFS+length(accINPUT_IFS)-1);
     % IFS acceleration data INPUT
% accRESPONSE_DFS=accRESPONSE(end_IFS:end_IFS+length(accINPUT_IFS)-1);
     % IFS acceleration data OUTPUT
else
    accINPUT_IFS=accINPUT(1:end);           % IFS acceleration data
 INPUT
    accRESPONSE_IFS=accRESPONSE(1:end);     % IFS acceleration data
 OUTPUT
    accINPUT_DFS=0;           % IFS acceleration data INPUT
    accRESPONSE_DFS=0;     % IFS acceleration data OUTPUT
end

l_IFS=length(accINPUT_IFS);
l_DFS=length(accINPUT_DFS);
f_IFS= Fs*(0:(l_IFS/2))/l_IFS;
f_DFS= Fs*(0:(l_DFS/2))/l_DFS;

%fft done for filtered acceleration data IFS
Yinput_IFS = fft(accINPUT_IFS);
P2input_IFS = abs(Yinput_IFS/l_IFS);
P1input_IFS = P2input_IFS(1:floor(l_IFS/2)+1);
P1input_IFS(2:end-1) = 2*P1input_IFS(2:end-1);
Yresponse_IFS = fft(accRESPONSE_IFS);
P2response_IFS = abs(Yresponse_IFS/l_IFS);
P1response_IFS = P2response_IFS(1:floor(l_IFS/2)+1);
P2aRESPONSE_IFS=P1response_IFS;
P1response_IFS(2:end-1) = 2*P1response_IFS(2:end-1);
```

```
%fft done for filtered acceleration data DFS
Yinput_DFS = fft(accINPUT_DFS);
P2input_DFS = abs(Yinput_DFS/l_DFS);
P1input_DFS = P2input_DFS(1:floor(l_DFS/2)+1);
P1input_DFS(2:end-1) = 2*P1input_DFS(2:end-1);
Yresponse_DFS = fft(accRESPONSE_DFS);
P2response_DFS = abs(Yresponse_DFS/l_DFS);
P1response_DFS = P2response_DFS(1:floor(l_DFS/2)+1);
P2aRESPONSE=P1response_DFS;
P1response_DFS(2:end-1) = 2*P1response_DFS(2:end-1);

%Transmissibility function for filtered data:
Tr_acc_IFS=P1response_IFS./P1input_IFS;
smo_Tr_IFS=smoothdata(Tr_acc_IFS,'movmedian',100);
Tr_acc_DFS=P1response_DFS./P1input_DFS;
smo_Tr_DFS=smoothdata(Tr_acc_DFS,'movmedian',100);

if length(accINPUT)>end_IFS
f1=f_IFS(2)-f_IFS(1);
freq1=f(40*(1/f1):60*(1/f1));
[maxIFS, imaxIFS]=max(smo_Tr_IFS(40*(1/f1):60*(1/f1)));
% [maxIFS, imaxIFS]=max(smo_Tr_IFS);
f_IFS_range=f_IFS(40*(1/f1):60*(1/f1));
xAtMaxIFS = f_IFS_range(imaxIFS);
fprintf('IFS: Max T=%f at %fHz\n',maxIFS,xAtMaxIFS)
f2=f_DFS(2)-f_DFS(1);
[maxDFS, imaxDFS]=max(smo_Tr_DFS(40*(1/f2):60*(1/f2)));
f_DFS_range=f_DFS(40*(1/f2):60*(1/f2));
xAtMaxDFS = f_DFS_range(imaxDFS);
fprintf('DFS: Max T=%f at %fHz\n',maxDFS,xAtMaxDFS)
else
    f1=f_IFS(2)-f_IFS(1);
    freq1=f(40*(1/f1):60*(1/f1));
    [maxIFS, imaxIFS]=max(smo_Tr_IFS(40*(1/f1):60*(1/f1)));
    % [maxIFS, imaxIFS]=max(smo_Tr_IFS);
    f_IFS_range=f_IFS(40*(1/f1):60*(1/f1));
    xAtMaxIFS = f_IFS_range(imaxIFS);
    fprintf('IFS: Max T=%f at %fHz\n',maxIFS,xAtMaxIFS)
end

% FFT FOR GAIN AND PHASE SHIFT-IFS
dataPsd0_IFS = fft((accINPUT_IFS-mean(accINPUT_IFS)), NFFT);
dataPsd1_IFS = fft((accRESPONSE_IFS-mean(accRESPONSE_IFS)), NFFT);
magTmp_IFS = abs(dataPsd1_IFS(1:floor(NFFT/2)+1)./
dataPsd0_IFS(1:floor(NFFT/2)+1));
phaseTmp_IFS = angle(dataPsd1_IFS(1:floor(NFFT/2)+1)./
dataPsd0_IFS(1:floor(NFFT/2)+1));

% FFT FOR GAIN AND PHASE SHIFT-DFS
dataPsd0_DFS = fft((accINPUT_DFS-mean(accINPUT_DFS)), NFFT);
dataPsd1_DFS = fft((accRESPONSE_DFS-mean(accRESPONSE_DFS)), NFFT);
magTmp_DFS = abs(dataPsd1_DFS(1:floor(NFFT/2)+1)./
dataPsd0_DFS(1:floor(NFFT/2)+1));
```

```
phaseTmp_DFS = angle(dataPsd1_DFS(1:floor(NFFT/2)+1)./
dataPsd0_DFS(1:floor(NFFT/2)+1));

freq=Fs/2*linspace(0,1,round(NFFT/2)+1);
smo_IFS1 = smoothdata(magTmp_IFS,'movmedian',100);
smo_DFS1 = smoothdata(magTmp_DFS,'movmedian',100);
```

Plotting the data

```
%Plot of the gain for IFS and DFS
if length(accINPUT)>end_IFS
figure (1)
plot(f_IFS,smo_Tr_IFS,'.',f_DFS,smo_Tr_DFS,'r.')
% plot(f_IFS,Tr_acc_IFS,'.',f_IFS,smo_Tr_IFS,'r.',...
%     f_DFS,Tr_acc_DFS,'.',f_DFS,smo_Tr_IFS,'r.')
xlabel('f[Hz]')
ylabel('Gain[/]')
xlim([20 60])
ylim([0 4])
% l = legend('\color{red} sin(x)','\color{blue} cos(x)');
legend({'\color{blue} IFS Gain','\color{red} DFS
 Gain'},'Location','northwest','FontSize',14)
set(get(gca,'title'),'Position',[40 3.3])
% title('BC50_{\mid\mid}','FontSize',24)
title('BC50_{\perp}','FontSize',24)
else
figure (1)
plot(f_IFS,smo_Tr_IFS,'.')
% plot(f_IFS,Tr_acc_IFS,'.',f_IFS,smo_Tr_IFS,'r.',...
%     f_DFS,Tr_acc_DFS,'.',f_DFS,smo_Tr_IFS,'r.')
xlabel('f[Hz]')
ylabel('Gain[/]')
xlim([20 60])
ylim([0 4])
% l = legend('\color{red} sin(x)','\color{blue} cos(x)');
legend({'\color{blue} IFS Gain'},'Location','northwest','FontSize',14)
set(get(gca,'title'),'Position',[40 3.3])
% title('BC50_{\mid\mid}','FontSize',24)
title('BC50_{\perp}','FontSize',24)
end
%Plot gain and phase
figure (2)
subplot (2,1,1)
plot(freq,smo_IFS1,'.',freq,smo_DFS1,'r.');
title('Gain')
xlabel('f[Hz]')
ylabel('Gain[/]')
xlim([10 100])
ylim([0 4])
legend('IFS gain','DFS gain')
subplot (2,1,2)
plot(freq,rad2deg(phaseTmp_IFS),'.',freq,rad2deg(phaseTmp_DFS),'r.');
title('Phase')
```

```
xlabel('f[Hz]')
ylabel('Phase[{\circ}]')
xlim(f_range)
legend('IFS phase shift','DFS phase shift')

%Plot of acceleration in time domain for input and response IFS and
 DFS seperately
P1input_IFS = smoothdata(P1input_IFS,'movmedian',100);
P1response_IFS = smoothdata(P1response_IFS,'movmedian',100);
P1input_DFS = smoothdata(P1input_DFS,'movmedian',100);
P1response_DFS = smoothdata(P1response_DFS,'movmedian',100);

figure(3)
plot(f_IFS,P1input_IFS,'.',f_IFS,P1response_IFS,'r.',...
    f_DFS,P1input_DFS,'k.',f_DFS,P1response_DFS,'g.')
title('INPUT and RESPONSE signals in frequency domain')
xlabel 'f (Hz)'
ylabel 'Acceleration[/]'
legend('Acceleration INPUT-IFS','Acceleration RESPONSE-
IFS','Acceleration INPUT-DFS','Acceleration RESPONSE-
DFS','Location','northwest')
grid on
xlim([20 60])

%Plots of RESPONSE in time domain
figure(4)
plot(t,OriginalOutput,'r.',t,OriginalInput,'k.');
title('Plots in time domain INPUT and RESPONSE')
xlabel 't[s]'
ylabel 'Acceleration[m/s^2]'
legend('Acceleration in time domain RESPONSE','Acceleration in time
 domain INPUT')

figure(5)
plot(t,accRESPONSE,'r.',t,accINPUT,'k.');
title('Plots in time domain for filtered INPUT and RESPONSE')
xlabel 't[s]'
ylabel 'Acceleration[m/s^2]'
legend('Acceleration in time domain filtered-RESPONSE','Acceleration
 in time domain filtered-INPUT')

% % split the IFS and DFS for the response in the time domain
% t_ifs1=t(1:length(accRESPONSE_IFS));
% t_dfs1=t(length(accRESPONSE_IFS):length(accRESPONSE_IFS)*2);
% figure(6)
% plot(t(1:length(accRESPONSE_IFS)),accRESPONSE_IFS,'.',...
% t(1:length(accINPUT_IFS)),accINPUT_IFS,'k.',...
%
 t(length(accRESPONSE_DFS):length(accRESPONSE_DFS)*2-1),accRESPONSE_DFS,'r.',...
%
 t(length(accRESPONSE_DFS):length(accRESPONSE_DFS)*2-1),accINPUT_DFS,'k.');
% title('Acceleration in time domain INPUT and RESPONSE for IFS and
 DFS')
% xlabel 't[s]'
```

```
% ylabel 'Acceleration[m/s^2]'
% xlim([0 inf])
% legend('RESPONSE-IFS','INPUT-IFS','RESPONSE-DFS','INPUT-DFS')
```

Published with MATLAB® R2018a

Bibliography

[1] Elaine Nicpon Marieb and Katja Hoehn. *Human anatomy physiology*. Pearson, Boston, MA, 9 edition, 2013.

[2] Les Barnsley. *4 - BACK PAIN*, pages 47–59. Churchill Livingstone, 2010.

[3] Gunnar B. J. Andersson. Epidemiological features of chronic low-back pain. *The Lancet*, 354(9178):581–585, 1999.

[4] José W. Geurts, Paul C. Willems, Jan-Willem Kallewaard, Maarten van Kleef, and Carmen Dirksen. The impact of chronic discogenic low back pain: Costs and patients' burden. *Pain research management*, 2018:4696180–4696180, 2018.

[5] Jeffrey Katz. Lumbar disc disorders and low-back pain: Socioeconomic factors and consequences. *The Journal of bone and joint surgery. American volume*, 88 Suppl 2:21–4, 2006.

[6] Michael Devereaux. Low back pain. *Medical Clinics of North America*, 93(2):477–501, 2009.

[7] S. Pahlavan, S. Berven, and S. S. Bederman. Variation in costs of spinal implants in united states academic medical centers. *Spine (Phila Pa 1976)*, 41(6):515–21, 2016.

[8] Mayfield Clinic. Anatomy of the spine. `https://mayfieldclinic.com/pe-anatspine.htm`. [Accessed: 2019-11-10].

[9] N. Newell, J. P. Little, A. Christou, M. A. Adams, C. J. Adam, and S. D. Masouros. Biomechanics of the human intervertebral disc: A review of testing techniques and results. *J Mech Behav Biomed Mater*, 69:420–434, 2017.

[10] F. Alonso and D. J. Hart. *Intervertebral Disk*, pages 724–729. Academic Press, Oxford, 2014.

[11] P. Prithvi Raj. Intervertebral disc: Anatomy-physiology-pathophysiology-treatment. *Pain Practice*, 8(1):18–44, 2008.

[12] Augustus A. White. *Clinical biomechanics of the spine*. Philadelphia, Pa. [etc.] : Lippincott, 2nd ed. edition, 1990.

[13] H. Lin, Y. K. Liu, and K. Adams. Mechanical response of the lumbar intervertebral joint under physiological (complex) loading. *The Journal of bone and joint surgery. American volume*, 60:41–55, 1978.

[14] M. D. Humzah and R. W. Soames. Human intervertebral disc: Structure and function. *The Anatomical Record*, 220(4):337–356, 1988.

[15] Gregory Plaugher and Mark Lopes. Clinical anatomy and biomechanics of the spine. *Textbook of clinical chiropractic: a specific biomechanical approach*, 1993.

[16] K. A. Tomaszewski, K. Saganiak, T. Gladysz, and J. A. Walocha. The biology behind the human intervertebral disc and its endplates. *Folia Morphol (Warsz)*, 74(2):157–68, 2015.

[17] Nikolai Bogduk. *Clinical anatomy of the lumbar spine and sacrum*. Edinburgh : Elsevier Churchill Livingstone, 4th ed. edition, 2005.

[18] Tomokazu Nakamura, Takaro Iribe, Yoshinori Asou, Hiroo Miyairi, Kozo Ikegami, and Kazuo Takakuda. Effects of compressive loading on biomechanical properties of disc and peripheral tissue in a rat tail model. *European spine journal : official publication of the European Spine Society, the European Spinal Deformity Society, and the European Section of the Cervical Spine Research Society*, 18(11):1595–1603, 2009.

[19] Bao-Gan Peng. Pathophysiology, diagnosis, and treatment of discogenic low back pain. *World journal of orthopedics*, 4(2):42–52, 2013.

[20] C.E. Badgley. The articular facets in relation to low-back pain and sciatic radiation. *Journal of Bone and Joint Surgery*, 23:481–496, 1941.

[21] Harold Merskey and Taxonomy International Association for the Study of Pain. Task Force on. *Classification of chronic pain : descriptions of chronic pain syndromes and definitions of pain terms*. Seattle : IASP, 2nd ed., repr. edition, 2002.

[22] H. V. Crock. A reappraisal of intervertebral disc lesions. *Medical Journal of Australia*, 1(20):983–989, 1970.

[23] K. R. Wade, P. A. Robertson, A. Thambyah, and N. D. Broom. How healthy discs herniate: A biomechanical and microstructural study investigating the combined effects of compression rate and flexion. *Spine*, 39(13):1018–1028, 2014.

[24] G. Marini, G. Huber, K. Puschel, and S. J. Ferguson. Nonlinear dynamics of the human lumbar intervertebral disc. *J Biomech*, 48(3):479–88, 2015.

[25] Physiopedia. File:disc extrusion.jpg — physiopedia,. `https://www.physio-pedia.com/index.php?title=File:Disc_extrusion.jpg&oldid=40928`, 2011. [Accessed: 2019-08-18].

[26] S. Asano, K. Kaneda, S. Umehara, and S. Tadano. The mechanical properties of the human l4-5 functional spinal unit during cyclic loading. the structural effects of the posterior elements. *Spine*, 17(11):1343–52, 1992.

[27] O. Izambert, D. Mitton, M. Thourot, and F. Lavaste. Dynamic stiffness and damping of human intervertebral disc using axial oscillatory displacement under a free mass system. *European Spine Journal*, 12(6):562–566, 2003.

[28] Virgin W. J. Experimental investigations into the physical properties of the intervertebral disc. *The Journal of Bone and Joint Surgery. British volume*, 33-B(4):607–611, 1951.

[29] John J. Costi, Ian A. Stokes, Mack G. Gardner-Morse, and James C. Iatridis. Frequency-dependent behavior of the intervertebral disc in response to each of six degree of freedom dynamic loading: Solid phase and fluid phase contributions. *Spine*, 33(16):1731–1738, 2008.

[30] W. Koeller, S. Muehlhaus, W. Meier, and F. Hartmann. Biomechanical properties of human intervertebral discs subjected to axial dynamic compression—influence of age and degeneration. *Journal of Biomechanics*, 19(10):807–816, 1986.

[31] Andrew J. L. Walsh and Jeffrey C. Lotz. Biological response of the intervertebral disc to dynamic loading. *Journal of Biomechanics*, 37(3):329–337, 2004.

[32] H. Seidel, R. Blüthner, B. Hinz, and M. Schust. On the health risk of the lumbar spine due to whole-body vibration—theoretical approach, experimental data and evaluation of whole-body vibration. *Journal of Sound and Vibration*, 215(4):723–741, 1998.

[33] M. KASRA, A. SHIRAZI-ADL, and G. DROUIN. Dynamics of human lumbar intervertebral joints: Experimental and finite-element investigations. *Spine*, 17(1):93–102, 1992.

[34] European Union. Directive 2002/44/ec of the european parliament and of the council. 2002.

[35] Khalid Malik and Ariana Nelson. *Overview of Low Back Pain Disorders*, pages 193–206.e2. 2018.

[36] E. A. Friis, A. K. Tsao, L. D. Timmie Topoleski, and L. C. Jones. *Introduction to mechanical testing of orthopedic implants*, pages 3–15. 2017.

[37] Weill Cornell Brain and Spine Center. Tlif minimally invasive spine fusion. `https://weillcornellbrainandspine.org/procedure/tlif-minimally-invasive-spine-fusion`. [Accessed: 2019-08-31].

[38] Gelenk-Klinik. Spinal disc replacement: supporting pain free mobility through next generation spinal prosthesis. `https://www.joint-surgeon.com/back-and-spine-specialist/artificial-disc-replacement-surgery.html`. [Accessed: 2019-12-22].

[39] W. H. Wagner, J. J. Regan, S. P. Leary, T. H. Lanman, J. P. Johnson, R. K. Rao, and D. V. Cossman. Access strategies for revision or explantation of the charite lumbar artificial disc replacement. *J Vasc Surg*, 44(6):1266–72, 2006.

[40] M. Skeppholm, T. Henriques, and T. Tullberg. Higher reoperation rate following cervical disc replacement in a retrospective, long-term comparative study of 715 patients. *Eur Spine J*, 26(9):2434–2440, 2017.

[41] Maurizio Genitiempo. *Biomaterial in spinal surgery*, pages 341–359. 2019.

[42] L. Wolfinbarger, Y. X. Zhang, B. L. T. Adam, V. Sutherland, K. Gates, and B. Brame. A comprehensive study of physical parameters, biomechanical properties, and statistical correlations of iliac crest bone wedges used in spinal-fusion surgery .2. mechanical-properties and correlation with physical parameters. *Spine*, 19(3):284–295, 1994.

[43] Ulrich Medical. Lumbar interbody fusion cage / anterior. `https://www.medicalexpo.com/prod/ulrich-medical/product-70397-723822.html`. [Accessed: 2019-12-27].

[44] Medtronic. Lumbar interbody fusion cage / anterior / pre-filled. `https://www.medicalexpo.com/prod/medtronic/product-70691-715295.html`. [Accessed: 2019-12-27].

[45] Y. Shikinami and M. Okuno. Mechanical evaluation of novel spinal interbody fusion cages made of bioactive, resorbable composites. *Biomaterials*, 24(18):3161–3170, 2003.

[46] T. Kauth, C. Hopmann, B. Kujat, F. W. Bach, B. Welke, C. Hurschler, K. Kalla, and D. Daentzer. Mechanical testing of an absorbable hybrid fusion cage for the cervical spine. *Biomedical Engineering-Biomedizinische Technik*, 57(5):353–358, 2012.

[47] Osseus. Aries. `https://osseus.com/aries-ibfd/`. [Accessed: 2019-08-31].

[48] Paul Egan, Xiuyu Wang, Helen Greutert, Kristina Shea, Karin Wuertz-Kozak, and Stephen Ferguson. Mechanical and biological characterization of 3d printed lattices. *3D Printing and Additive Manufacturing*, 6(2):73–81, 2019.

[49] P. F. Egan, V. C. Gonella, M. Engensperger, S. J. Ferguson, and K. Shea. Computationally designed lattices with tuned properties for tissue engineering using 3d printing. *PLoS One*, 12(8):e0182902, 2017.

[50] Paul F. Egan, Isabella Bauer, Kristina Shea, and Stephen J. Ferguson. Mechanics of three-dimensional printed lattices for biomedical devices. *Journal of Mechanical Design*, 141(3), 2019.

[51] Paul F. Egan, Stephen J. Ferguson, and Kristina Shea. Design of hierarchical three-dimensional printed scaffolds considering mechanical and biological factors for bone tissue engineering. *Journal of Mechanical Design*, 139(6), 2017.

[52] M. Sanami. *Auxetic Materials for Biomedical Applications*. University of Bolton, 2015.

[53] C.E. Baker. *Auxetic Spinal Implants: Consideration of Negative Poisson's Ratio in the Design of an Artificial Intervertebral Disc*. University of Toledo, 2011.

[54] Sukhwinder K. Bhullar. Characterization of auxetic polyurethanes foam for biomedical implants. *e-Polymers*, 14(6):441–447, 2014.

[55] Li Yang, Ola Harrysson, Harvey West, and Denis Cormier. Design and characterization of orthotropic re-entrant auxetic structures made via ebm using ti6al4v and pure copper. *22nd Annual International Solid Freeform Fabrication Symposium - An Additive Manufacturing Conference, SFF 2011*, pages 464–474, 2011.

[56] ASTM International. F2077-18 test methods for intervertebral body fusion devices. *ASTM International*, 2018.

[57] C. Caparros, J. Guillem-Marti, M. Molmeneu, M. Punset, J. A. Calero, and F. J. Gil. Mechanical properties and in vitro biological response to porous titanium alloys prepared for use in intervertebral implants. *Journal of the Mechanical Behavior of Biomedical Materials*, 39:79–86, 2014.

[58] H. S. Li, X. N. Zou, C. Woo, M. Ding, M. Lind, and C. Bunger. Experimental lumbar spine fusion with novel tantalum-coated carbon fiber implant. *Journal of Biomedical Materials Research Part B-Applied Biomaterials*, 81B(1):194–200, 2007.

[59] V. Ella, M. Kellomaki, and P. Tormala. In vitro properties of plla screws and novel bioabsorbable implant with elastic nucleus to replace intervertebral disc. *Journal of Materials Science-Materials in Medicine*, 16(7):655–662, 2005.

[60] H. Murakami, W. C. Horton, K. Tomita, and W. C. Hutton. A two-cage reconstruction versus a single mega-cage reconstruction for lumbar interbody fusion: an experimental comparison. *Eur Spine J*, 13(5):432–40, 2004.

[61] S. M. R. Moeini, R. J. Nasca, J. E. Lemons, and R. D. Montgomery. Intervertebral spacer as an adjunct to anterior lumbar fusion. part i. design, fabrication, and testing of three prototypes. *Journal of Spinal Disorders*, 11(2):129–135, 1998.

[62] P. F. Egan, K. A. Shea, and S. J. Ferguson. Simulated tissue growth for 3d printed scaffolds. *Biomech Model Mechanobiol*, 2018.

[63] Giacomo Marini, Gerd Huber, Klaus Püschel, and Stephen J. Ferguson. A 1-d model of the nonlinear dynamics of the human lumbar intervertebral disc. *Journal of Sound and Vibration*, 387:194–206, 2017.

[64] G. Marini and S. J. Ferguson. Nonlinear numerical analysis of the structural response of the intervertebral disc to impact loading. *Comput Methods Biomech Biomed Engin*, 17(9):1002–11, 2014.

[65] Paul Egan, Veronica Gonella, Max Engensperger, Stephen Ferguson, and Kristina Shea. *Design and Fabrication of 3D Printed Tissue Scaffolds Informed by Mechanics and Fluids Simulations*. 2017.

[66] Stratasys. Objet350 and objet500 connex3 spec sheet. 2016.

[67] Paul Egan, X Wang, H Greutert, K Shea, K Wuertz-Kozak, and Stephen Ferguson. Mechanical and biological characterization of 3d printed lattices. *3D Printing and Additive Manufacturing*, 6:73–81, 04 2019.

[68] Pei-I. Tsai, Ching-Chi Hsu, San-Yuan Chen, Tsung-Han Wu, and Chih-Chieh Huang. Biomechanical investigation into the structural design of porous additive manufactured cages using numerical and experimental approaches. *Computers in Biology and Medicine*, 76, 2016.

[69] M. van Dijk, T. H. Smit, S. Sugihara, E. H. Burger, and P. I. Wuisman. The effect of cage stiffness on the rate of lumbar interbody fusion: an in vivo model using poly(l-lactic acid) and titanium cages. *Spine (Phila Pa 1976)*, 27(7):682–8, 2002.